

A palette of bridged bicycle-strengthened fluorophores

Received: 20 September 2024

Accepted: 3 April 2025

Published online: 19 May 2025

 Check for updates

Junwei Zhang¹, Kecheng Zhang¹, Kui Wang², Bo Wang^{3,4}, Siyan Zhu^{3,5}, Hongping Qian⁶, Yumiao Ma⁷, Mengling Zhang¹, Tianyan Liu¹, Peng Chen^{8,9}, Yuan Shen³, Yunzhe Fu¹⁰, Shilin Fang², Xinxin Zhang^{2,11}, Peng Zou^{3,5,12}, Wulan Deng^{3,4,13}, Yu Mu^{2,14} & Zhixing Chen^{1,3,8} ✉

Organic fluorophores are the keystone of advanced biological imaging. The vast chemical space of fluorophores has been extensively explored in search of molecules with ideal properties. However, within the current molecular constraints, there appears to be a trade-off between high brightness, robust photostability, and tunable biochemical properties. Herein we report a general strategy to systematically boost the performance of donor-acceptor-type fluorophores, such as rhodamines, by leveraging SO₂ and O-substituted azabicyclo[3.2.1]octane auxochromes. These bicyclic heterocycles give rise to a collection of ‘bridged’ dyes (BD) spanning the ultraviolet and visible range with top-notch quantum efficiencies, enhanced water solubility, and tunable cell-permeability. Notably, these azabicyclic fluorophores showed remarkable photostability compared to their tetramethyl or azetidinium analogs while being completely resistant to oxidative photobleaching. Functionalized BD dyes are tailored for applications in single-molecule imaging, super-resolution imaging (STED and SIM) in fixed or live mammalian and plant cells, and live zebrafish imaging and chemogenetic voltage imaging.

In the past two decades, advanced fluorescence imaging techniques, with spatial resolution surpassing the Abbe diffraction limit and a near-millisecond temporal resolution, have become routine tools in biological research^{1–4}. In parallel, the expanding palette of organic fluorophores^{5–8} and modern labeling strategies^{9–12} are increasingly replacing fluorescent proteins^{13,14} to meet the growing demand for four-dimensional (4D) (three dimensions (3D) plus time-lapse) imaging while optimizing photon budgets and enabling

multiplexed labeling. An ideal fluorophore for contemporary imaging technologies would feature high brightness; superior photophysical, chemical, and spectral stability; tailored hydrophilicity; and excellent biocompatibility with and without excitation light. However, state-of-the-art fluorescent tools often have to compromise to balance all these characteristics. In other words, the quest for dyes with ideal properties calls for the exploration of a broader chemical space¹⁵.

¹College of Future Technology, Institute of Molecular Medicine, National Biomedical Imaging Center, Beijing Key Laboratory of Cardiometabolic Molecular Medicine, State Key Laboratory of Membrane Biology, Peking University, Beijing, China. ²Institute of Neuroscience, State Key Laboratory of Neuroscience, Center for Excellence in Brain Science and Intelligence Technology, Chinese Academy of Sciences, Shanghai, China. ³Peking-Tsinghua Center for Life Sciences, Academy for Advanced Interdisciplinary Studies, Peking University, Beijing, China. ⁴Biomedical Pioneering Innovation Center (BIOPIC), Peking University, Beijing, China. ⁵College of Chemistry and Molecular Engineering, Synthetic and Functional Biomolecules Center, Beijing National Laboratory for Molecular Sciences, Key Laboratory of Bioorganic Chemistry and Molecular Engineering of Ministry of Education, PKU-IDG/McGovern Institute for Brain Research, Peking University, Beijing, China. ⁶College of Biological Sciences and Biotechnology, Beijing Forestry University, Beijing, China. ⁷BSJ Institute, Beijing, China. ⁸PKU-Nanjing Institute of Translational Medicine, Nanjing, China. ⁹Genvivo Biotech, Nanjing, China. ¹⁰Department of Biomedical Engineering, College of Future Technology, Peking University, Beijing, China. ¹¹ShanghaiTech University, Shanghai, China. ¹²Chinese Institute for Brain Research (CIBR), Beijing, China. ¹³Beijing Advanced Innovation Center for Genomics (ICG), Peking University, Beijing, China. ¹⁴University of Chinese Academy of Sciences, Beijing, China. ✉e-mail: zhixingchen@pku.edu.cn

The structural and electronic properties of auxochromes are crucial to photophysical and chemical properties of the donor–acceptor-type (D-A type) fluorophores. Early designs generally improved the performance of fluorophores through structural rigidification and sulfonation (for example, Alexa Fluor¹⁶ and ATTO Dyes (<https://www.atto-tec.com/produkte/Fluorescent-Labels/>)). These classic compounds are still mainstays in the field of immunofluorescence. In parallel, as live-cell imaging and bio-orthogonal labeling strategies started to take the stage, a new trend of auxochrome engineering emerged, aiming to suppress the formation of twisted intramolecular charge transfer (TICT) to enhance brightness (Fig. 1a,b)^{17,18}. In 2008, the Foley group reported 7-azabicyclo[2.2.1]heptane as an auxochrome moiety with a small steric hindrance that can inhibit the TICT state¹⁹. This design utilized bridgehead carbon, which cannot form double bonds, to prevent the generation of photo-oxidation intermediates and eliminate photobleaching. More recently, the Lavis group systematically engineered azetidines substituted fluorophores, dubbed JF dyes^{20–22}, which greatly improved brightness while preserving compatibility with self-labeling protein tags^{23,24}. JF dyes have now become a popular tool for live-cell and in vivo labeling. Yet, owing to the high ring tensile force of azetidines and the presence of α -H atoms, their photobleaching (photophysical stability) and photobleaching (spectral stability) are evident, particularly under intense microscope lights^{25,26}. Subsequently, deuterated auxochromes were created by the Lavis group²⁷ and the Broichhagen group²⁸ to improve photostability and spectral stability. Meanwhile, new strategies to prevent TICT state by adjusting electronic effects were reported by the Xiao²⁹ and Guo³⁰ groups. Although the fluorescence quantum yields of these dyes are close to the theoretical limit, their photostability drastically decreased. At the same time, the Hell group reported triarylmethane fluorophores with auxochromes lacking α -H, which can effectively resist oxidative photobleaching at the cost of installing a bulky yet hydrophobic tert-butyl group³¹. In addition to issues of brightness and photostability, the water solubility and biocompatibility of fluorophores are gradually receiving more attention. The Gibbs group introduced a negatively charged sulfonate moiety to balance the cationic charge of rhodamine scaffolds to obtain a series of ORFluors with improved hydrophilicity while maintaining photophysical properties and cell permeability³². Along the line of auxochrome engineering, our group leveraged the hydrophilic morpholino auxochromes^{33,34} to address the nonspecific membrane staining issue of soluble Zinc indicators, enabling multiplexed time-lapse imaging of orchestrated insulin secretion³⁵. Although we are aware that the morpholino auxochromes compromise the brightness of rhodamine dyes, this initiative prompted us to further develop the next-generation molecular motifs that can generally produce dyes with high brightness, high photostability, and spectral stability, yet customizable hydrophilicity.

Here we report a palette of bridged bicycle-strengthened fluorophores (BriDye (BD)) with improved quantum efficiencies and uncompromised photo- and spectral stability that spans the ultraviolet (UV) and visible range. The BD family is composed of two series of fluorophores using SO₂- or O-substituted azabicyclo[3.2.1] octane auxochromes. Both dyes exhibit excellent photophysical properties while functionalized derivatives of BD dyes possess different hydrophilicity and membrane permeability to meet the demands of in vitro bioconjugation and live-cell protein labeling, respectively. By analyzing the crystal structure of the BD dye–protein binding complex, we have discovered new polar interactions between auxochromes and protein residues. We also showcase that BD dyes are suitable for hybrid sensors and functional neuronal imaging. Furthermore, bioavailable BD dyes showed outstanding performance on general state-of-the-art imaging technologies (including, but not limited to, single-molecule imaging, stimulated emission depletion microscopy, and structured illumination microscopy) in fixed and live mammalian cells, plant cells, and live animals for structural imaging.

Results

Rational design of bridged bicycle-strengthened fluorophores

We seek to synergistically integrate the biocompatibility of morpholino auxochrome, the brightness of azetidines or pyrrolidines auxochrome, and the photostability and spectral stability of bridged 7-azabicyclo[2.2.1]heptane auxochrome. Along this line, we speculate that SO₂- or O-substituted azabicyclo[3.2.1] octane³⁶ is a viable auxochrome with synthetic accessibility³⁶ (Fig. 1b). These designs are expected to bring the following benefits: (1) the electron-withdrawing groups substituted bridged bicyclic systems can optimize both steric hindrance^{19,20} and electronic effects^{29,30} to prevent the formation of the TICT state, thereby enhancing the brightness and photostability; (2) following Bredt's rule, in which a carbon double bond cannot occur at the branching position of the bridgeheads³⁷, the radical cation and iminium intermediates will be energetically unfavored during photo-oxidation, inhibiting this major photobleaching-photobleaching pathway; and (3) two types of auxochromes contain different hydrogen-bond acceptors that will render the dyes customizable hydrophilicity and membrane permeability for various applications. Before the chemical synthesis and characterization, we first examined these two auxochromes in silico on rhodamine scaffold, the most popular D-A type fluorophores in biological imaging. First, we characterized the steric hindrance effect of the auxochromes by the value of the C₁–N–C_n bond angle. The steric congestion of the two [3.2.1] bridged bicyclic rings was lower than that of *N,N*-dimethyl auxochromes or deuterated pyrrolidines but higher than that of azetidines or azabicyclo[2.2.1] heptane moieties (Fig. 1c). Next, we evaluated their electron-donating capacity by calculating their vertical ionization energies (VIEs) (Fig. 1c), revealing that two [3.2.1] bridged bicyclic rings have higher VIEs than do other moieties. This suggests that they are less electron-rich and more resistant to potential single electron oxidation. Finally, we calculated the potential energy surfaces of TMR, JF549, JFX554, and [2.2.1]R in water, and did the same for BD528 and BD555, as a function of auxochrome rotation angle (Fig. 1c and Supplementary Fig. 1). Our results suggested that the TICT pathway is inhibited by a larger rotational barrier (E_{RB}) in BD528/BD555 (0.46 eV and 0.43 eV, respectively) than that in TMR/JF549/JFX554/[2.2.1]R (0.18 eV, 0.10 eV, 0.20 eV, and 0.35 eV, respectively). In addition, the TICT state of BD528/BD555 does not form a minimum on the excited state potential energy surface, resulting in a positive driving energy (E_{DE}), meaning that these two fluorophores are energetically prohibited from transitioning into their TICT state³⁸, rendering the fluorescence emission their main pathway and resulting in high fluorescence quantum yields.

Photophysical properties of BD dyes in aqueous buffer

Encouraged by our results, we installed the above auxochromes into different scaffolds including coumarin, rhodamine, carbon-rhodamine, oxazine, and silicon-rhodamine classes, forming a palette of BD dyes spanning the UV and visible range with different photophysical properties (Fig. 1d). BD dyes are generally synthesized in a modular fashion. Starting from reported aryl triflates intermediates, we used the Buchwald–Hartwig cross-coupling approach to install the corresponding azabicyclo[3.2.1]octane in coumarin, rhodamine, carbon-rhodamine, and oxazine fluorophores³⁴ (Supplementary Scheme 1a–c). For silicon-rhodamine derivatives, the bicycles were introduced early in the synthetic route through the Buchwald–Hartwig reaction, followed by Friedel–Crafts type cyclization to yield the silicon-rhodamine chromophore³⁹ (Supplementary Scheme 1d–f).

We then measured the photophysical properties of these BD dyes and compared them with *N,N*-dialkyl analogs in aqueous buffer (Table 1 and Supplementary Fig. 2). On coumarin scaffolds, BD350 and BD356 exhibited significantly increased fluorescence quantum yield (13.7-fold and 10.3-fold respectively), lifetime, and blue-shifted absorption spectrum compared to coumarin 460. On rhodamine scaffolds, BD528 bearing SO₂-substituted azabicyclo[3.2.1]octane auxochromes exhibit

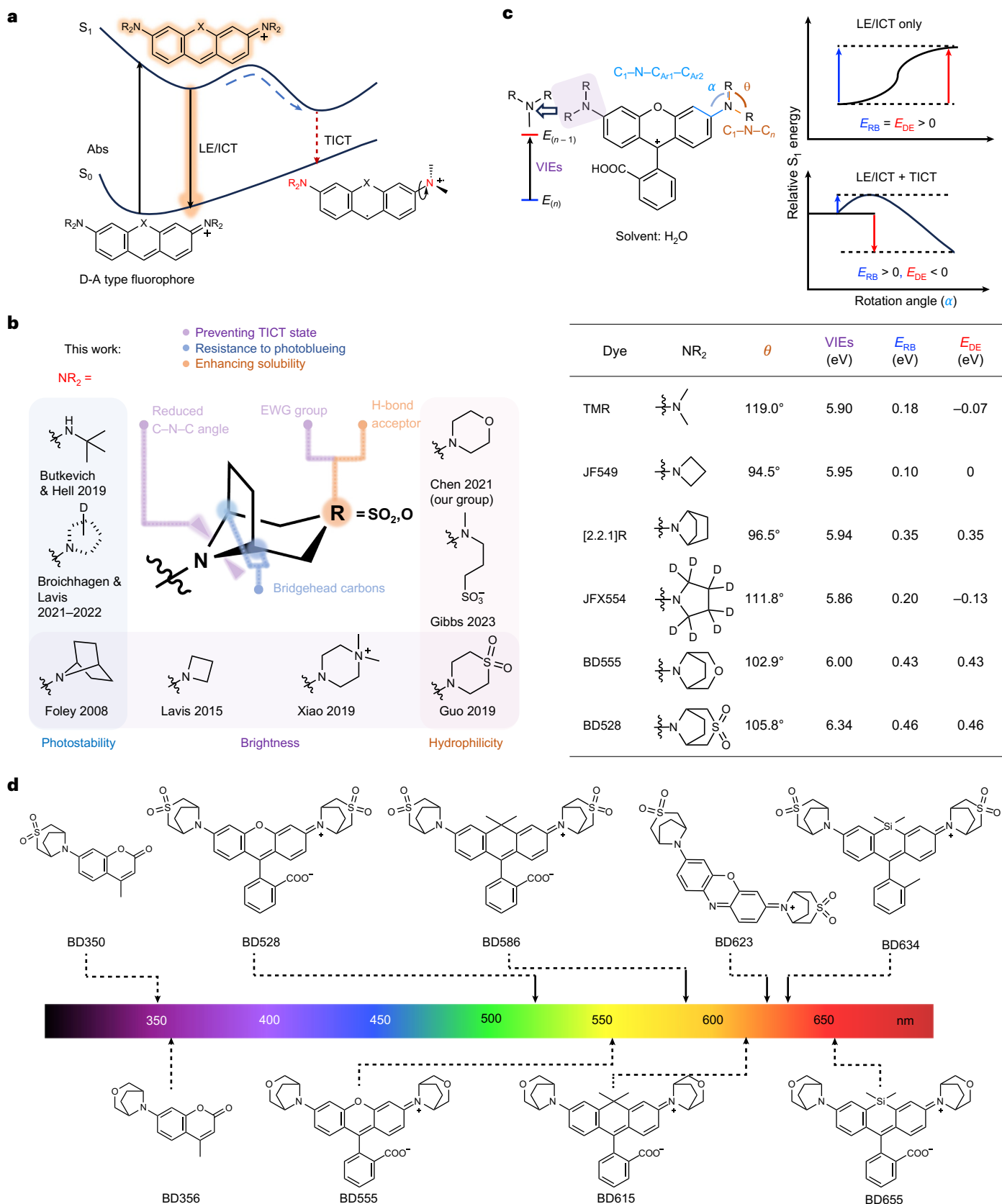


Fig. 1 | Development of fluorophores with bridged bicyclic auxochromes. **a**, The TICT mechanism. LE/ICT, local excited state and intermolecular charge transfer. **b**, Selected auxochromes and their properties. **c**, Theoretical models and calculation results. θ , the value of C_1-N-C_n bond angle; α , the value of

$C_1-N-C_{Ar1}-C_{Ar2}$ dihedral angle; E_{RB} , rotation barrier; E_{DE} , driving energy; $E_{(n)}$, electronic energy in neutral state; $E_{(n-1)}$, electronic energy in ionized state; VIE, $E_{(n-1)} - E_{(n)}$. **d**, Structures of the BD dye palette.

Table 1 | Photophysical properties of fluorophores^a

Prototype structure	Dye	Auxochrome NR ₂ =	λ_{abs} (nm)	λ_{em} (nm)	ϵ (M ⁻¹ cm ⁻¹)	ϵ_{max} (M ⁻¹ cm ⁻¹) ^b	Φ	τ (ns)	$K_{\text{L-Z}}$ ^c
	BD350		350	444	19,000	20,000	0.96	3.9	-
	BD356		356	474	21,000	29,000	0.72	4.2	-
	Coumarin 460		383	472	28,000	28,000	0.07	0.6	-
	BD528		528	554	93,000	143,000	0.98	4.0	0.090
	BD555		555	587	97,000	120,000	0.79	3.6	2.6
	TMR		548	572	80,000	114,000	0.43	2.3	4.1
	BD586		586	610	2,100	152,000	0.90	4.2 ^b	0.0012
	BD615		615	646	61,000	138,000	0.65	3.7	0.019
	CPY		606	628	100,000	128,000	0.54	3.3	0.85
	BD623		623	648	100,000	105,000	0.36	2.9	-
	Oxazine 1		654	669	101,000	102,000	0.09	0.7	-
	BD634		634	652	128,000	136,000	0.60	4.2	-
	SiTMR		648	662	116,000	124,000	0.31	2.7	-
	BD655		655	680	1,400	158,000	0.37	3.7 ^b	<0.0010
	SiR		644	663	26,200	139,000	0.39	3.5 ^b	0.0036

^aUnless noted, properties were measured in HEPES buffer (10 mM; pH, 7.3). ^bMeasured in ethanol containing 0.1% trifluoroacetic acid (coumarin, oxazine, and Si-rhodamine) or in ethanol containing 0.1% 2,2,2-trifluoroethanol (O- and C-rhodamine). ^cEquilibrium constant measured in 1:1 (vol/vol) dioxane/water. ϵ , extinction coefficient; Φ , fluorescence quantum yield; τ , fluorescence lifetime.

quantum yields close to the theoretical limit (98%), blue-shifted spectra (absorption wavelength (λ_{abs})/emission wavelength (λ_{em}) = 528/554 nm), and reduced lactone-zwitterion equilibrium constant ($K_{\text{L-Z}}$ = 0.090); BD555 containing O-substituted azabicyclo[3.2.1]octane auxochromes exhibited 1.8-fold increases in quantum yield and bathochromic shift in absorption maximum and emission maximum ($\lambda_{\text{abs}}/\lambda_{\text{em}}$ = 555/587 nm). Compared to [2.2.1]Rhod and TMR, BD555 and BD528 also exhibited significantly improved water solubility (Supplementary Fig. 3). The bridge auxochromes also showed a similar trend on the carbon-rhodamine scaffold. Notably, the lower apparent extinction coefficients and $K_{\text{L-Z}}$ the compounds BD586 and BD615 indicated a greater tendency toward their nonfluorescent lactone form in aqueous buffer. The SO₂-substituted azabicyclo[3.2.1]octane moiety on BD623 for oxazine and BD634 for monomethyl-substituted silicon-rhodamine scaffolds

also exhibited markedly high fluorescence quantum yield (36% and 60%, respectively). Furthermore, the O-substituted azabicyclo[3.2.1]octane moiety on BD655 for carboxyl-substituted silicon-rhodamine scaffolds showed a bathochromic shift in absorption and emission spectrum ($\lambda_{\text{abs}}/\lambda_{\text{em}}$ = 655/680 nm) and smaller $K_{\text{L-Z}}$ (<0.0010 versus 0.0036), suggesting that it could be a better far-red fluorogenic labeling for protein tags. Overall, the bridge auxochromes generally improve the fluorescence quantum yield of commonly used chromophores to a remarkably high level.

Photostability of BD dyes in aqueous buffer

The main known photobleaching pathway for rhodamine dyes is oxidative dealkylation at the N atom. Under irradiation and in oxygen-containing environments, this process progresses through

several stages: the formation of a radical cation, an α -aminoalkyl radical, and an iminium cation, which is eventually hydrolyzed to yield an aldehyde and a dealkylated dye (Fig. 2a). Each step of the dealkylation process will result in a blue shift of 10–15 nm in the absorption spectrum. These photodegradation reactions not only reduce the total photon budget, but also cause spectral shift into shorter wavelength channels, complicating data analysis in multiplexed imaging^{25,26,40}.

Bredt's rule suggests that double bonds are not favored at the bridgehead carbon, implying that the bridged bicyclic auxochrome prohibits the formation of the radical cation and iminium intermediate, blocking the dealkylative photobleaching and photobleuing pathways. We monitored the photobleaching process of BD dyes and other state-of-the-art fluorophores in aqueous buffer using UV-vis spectroscopy (Fig. 2b). The bridge bicyclic dyes BD528 and BD555 exhibited the best photostability and spectral stability, with distinct nonphotobleuing features (Fig. 2d,e). By contrast, other rhodamine dyes undergo varying degrees of photobleuing (Fig. 2f–i). The photobleaching rate of BD528 in aqueous solutions is slower than that of JF525 and Rhod524 (by 5.1-fold and 9.2-fold, respectively) (Fig. 2c). BD555 also exhibited a strong photostability advantage compared to TMR and JF549 (by 1.8-fold and 3.2-fold, respectively) (Fig. 2c). Notably, electron-withdrawing groups significantly reduced the photobleuing rate (comparing JF525 and Rhod524 versus JF549), but this phenomenon seems to be independent of the photobleaching process. On the red-shifted carbon-rhodamine scaffold, the bridged bicyclic fluorophore BD615 also shows improved photostability and spectral stability compared to CPY (Figs. 2c,j,k). It is also worth noting that the reactive aldehyde species derived from the oxidative photobleuing byproducts will contribute to cross-linking reactivity with proteins. In an *in vitro* test, we irradiated bluing (JF549) and nonbluing (BD555) fluorophores in air-saturated PBS buffer with bovine serum albumin (BSA) for 30 min. SDS-PAGE analysis showed the formation of covalent dye-BSA conjugates with JF549, whereas BD555 did not exhibit this reaction (Fig. 2l). These experiments underscore the advantages of nonphotobleuing dyes for labeling biomacromolecules.

BD derivatives in immunofluorescence imaging

Encouraged by the excellent photophysical properties of BD dyes, we tested their application in immunofluorescence. Besides brightness and photostability, a key factor for this technique is achieving a high degree of labeling on secondary antibodies, which requires superb solubility and minimal aggregation in aqueous environments^{41,42}. Traditionally, such solubilization has been achieved through sulfonation. We envisioned that BD dyes bearing sulfones in their bridged bicycles are ideal candidates, as the neutral sulfones provide high solubility without introducing excessive charges that could hamper protein functions. To this end, the *ortho*-carboxyl groups on the pendant ring of BD rhodamines were functionalized with 4-(methylamino) butanoic acid as coupling handles (Fig. 3a and Supplementary Scheme 2). Notably, this modification results in a bathochromic shift in the absorption/emission spectrum (~15 nm), while locking the chromophore in the open form, as characterized by an increase in extinction coefficient (Fig. 3b and Supplementary Fig. 4). In photostability tests (Fig. 3c and Supplementary Fig. 5), BD Yellow showed 2.7-fold-higher photostability than ATTO 532, with distinctive spectral stability (that is, no photobleuing) (Fig. 3c and Supplementary Fig. 5c,d). BD Orange and ATTO 594 exhibited similar photostability (Fig. 3d and Supplementary Fig. 5e,f). Atto 647N, one of the most popular dyes for single-molecule and super-resolution microscopy, showed significant blue shift after irradiation, whereas BD Red was a nonphotobleuing dye with 8.0-fold-higher photostability (Fig. 3e and Supplementary Fig. 5g,h).

Then, the amino-reactive *N*-hydroxysuccinimide (NHS) esters of BD Yellow, Orange, and Red were synthesized and conjugated with goat anti-mouse secondary antibodies. The labeling degrees were 3.27, 2.63, and 2.42, respectively, showcasing their excellent solubility. BriDyes

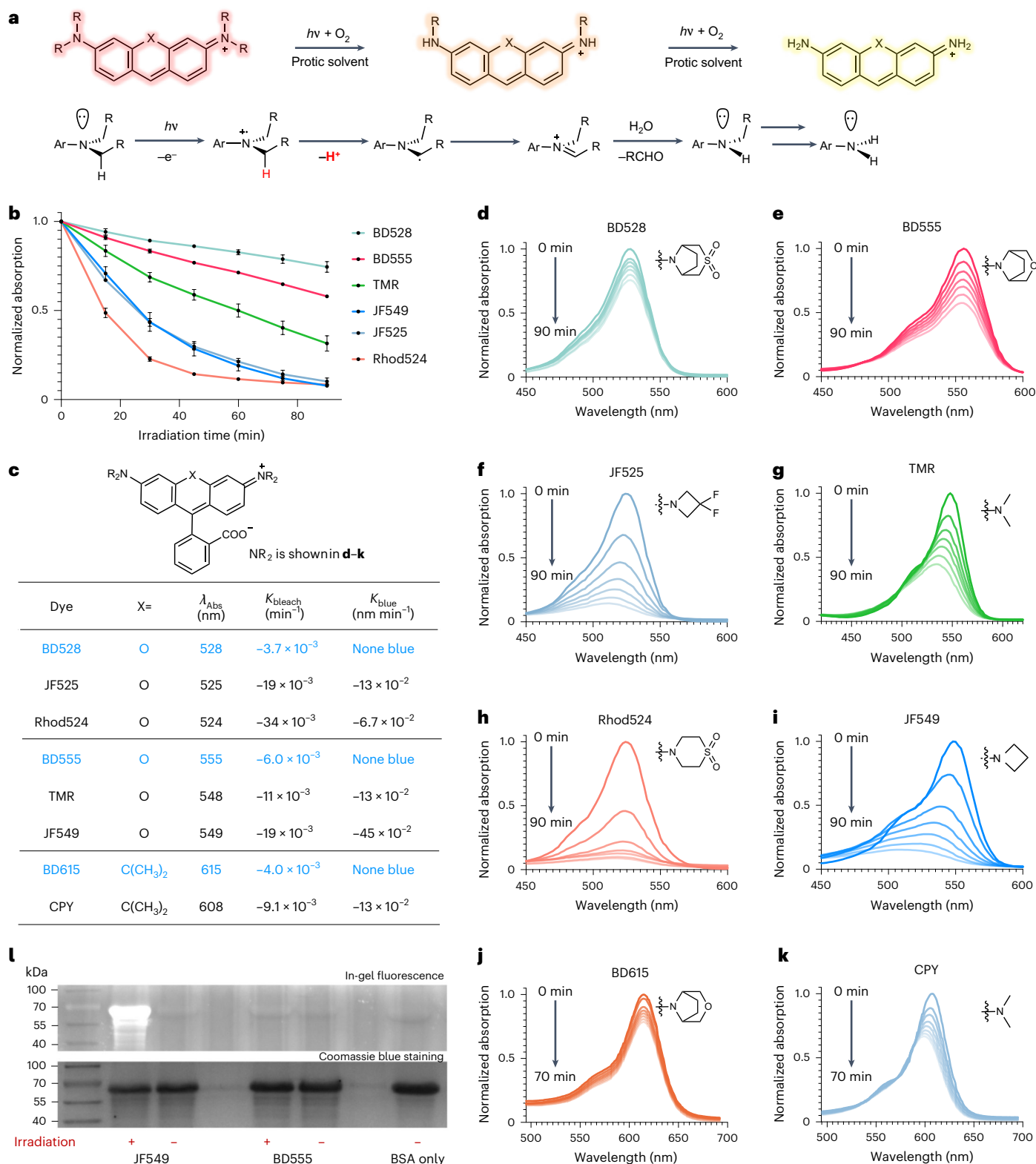
still outperformed their ATTO counterparts in photostability when conjugated to antibodies (Supplementary Fig. 6). Immunofluorescence imaging of lamin-A/C and α -tubulin using BD Yellow, BD Orange, and BD Red yielded strong signals in confocal mode (Fig. 3f–h). Owing to their photostability, BD Orange and BD Red are compatible with stimulated emission depletion microscopy (STED) imaging using a 775-nm depletion laser (Fig. 3g,h). Single microtubules can be resolved with a resolution under 80 nm (Fig. 3h,i), and the ultimate resolution can reach 30 nm (Supplementary Fig. 7). Overall, bridged bicyclic rhodamines are new additions to the toolkit for STED immunofluorescence imaging.

BD dyes synergize with HaloTag *in vitro* and *in cellulo*

To evaluate the compatibility of BD derivatives in live-cell imaging, we coupled HaloTag ligands with BD555, BD615, and BD655, which exhibit moderate hydrophilicity and suitable K_{LZ} ratios for cell membrane penetration (Fig. 4a and Supplementary Scheme 3). Upon binding with purified HaloTag7 protein, the three BD_{HTL} derivatives showed a marked increase in both the absorption and emission spectrum (Fig. 4b and Supplementary Fig. 8), indicating that the protein environment has a profound influence on both K_{LZ} and the fluorescence properties. In contrast to their *N,N*-dimethyl or azetidene-containing analogs, these BD_{HTL} derivatives showed a bathochromic shift in absorption spectra around 8–13 nm and emission spectra around 16–22 nm upon binding to HaloTag. So we renamed these HaloTag ligands on the basis of their maximum absorption after binding to protein (for example, BD555 to BD566_{HTL} and so on). BD566_{HTL} and BD626_{HTL} are among the brightest labels in their respective 561 and 640 channels, with extinction coefficients higher than 100,000 M⁻¹ cm⁻¹ and quantum yields higher than 0.80 after binding to HaloTag7. BD666_{HTL} showed a 40× increase in absorption and a 70× increase in emission (Fig. 4m and Supplementary Fig. 8e,f) upon HaloTag binding, which is more fluorogenic than the widely used far-red dye SiR_{HTL}⁴³ (4.8× increase in absorption and 15× increase in emission).

To better understand the interplay between BD_{HTL} dyes and HaloTag protein, we obtained a single BD626_{HTL} crystal at the pocket of HaloTag7, and its structure was solved at 1.7-Å resolution (Protein Data Bank (PDB): 9JHA). Compared to its *N,N*-dimethyl analog CPY_{HTL}-bound HT7 (PDB: 6Y7B, at 3.1-Å resolution)^{44,45}, the pockets in which the dyes reside are generally similar (Extended Data Fig. 1a). In both CPY_{HTL}- and BD626_{HTL}-bound HT7, T172 and T148 engage with the oxygen and the nitrogen of the amide bond linking the HaloTag ligands to the fluorophore (Extended Data Fig. 1b,c). Yet the positions and angles of chromophores on the HT7 protein are slightly different (Extended Data Fig. 1d). Notably, the distance from an O-substituted azabicyclo[3.2.1]octane on BD626_{HTL} to the amide side chain of Q165 is only 2.8 Å (Fig. 4c), indicating an active polar interaction (2.5 Å–3.5 Å) that is absent in its CPY_{HTL} counterpart. This polar interaction suggests that the hydrogen-bond acceptor on the auxochrome of fluorophore brings up new interaction sites with protein residues, giving new biochemical space for further protein engineering for advanced applications, such as chemogenetic hybrid sensors^{46,47}.

Next, we evaluated the performance of BD_{HTL} at the single-molecule level in a cellular context. To achieve sparse labeling for single-molecule detection, we used a high dilution of HaloTag ligands (2.5 pM) on live U2OS cells stably expressing H2B-HaloTag7 to ensure sparse labeling for single-molecule detection, followed by paraformaldehyde fixation. Continuous imaging of single molecules was conducted using total internal reflection fluorescence microscopy with highly inclined thin illumination (HiLo)⁴⁸ (Fig. 4d and Supplementary Video 1). BD566_{HTL} labeling exhibited the highest localization counts (Supplementary Fig. 9a), featuring a 1.19- and 1.85-fold increase of single-molecule brightness compared to JF549_{HTL} and TMR_{HTL} labeling, respectively (Fig. 4e). Moreover, BD566_{HTL} exhibited the best photostability among the three dyes in single-molecule experiments (Supplementary Fig. 9b), consistent with bulk *in vitro* measurements (Fig. 2d). Owing to the



d–k, The absorption of dyes over time. **l**, Photocrosslinking is a downstream side reaction of photo-oxidation. Solutions of fluorophores (10 μM in 0.1% (vol/vol) DMSO–PBS, pH 7.4, air-saturated) were irradiated in the presence of BSA (1 mg ml^{-1} , 25 $^{\circ}\text{C}$, 30 min) with a LED lamp (0.5 W cm^{-2} , 520–530 nm). The incubated samples were analyzed using in-gel fluorescence and Coomassie blue staining under denaturing conditions (SDS–PAGE). This experiment was independently repeated three times.

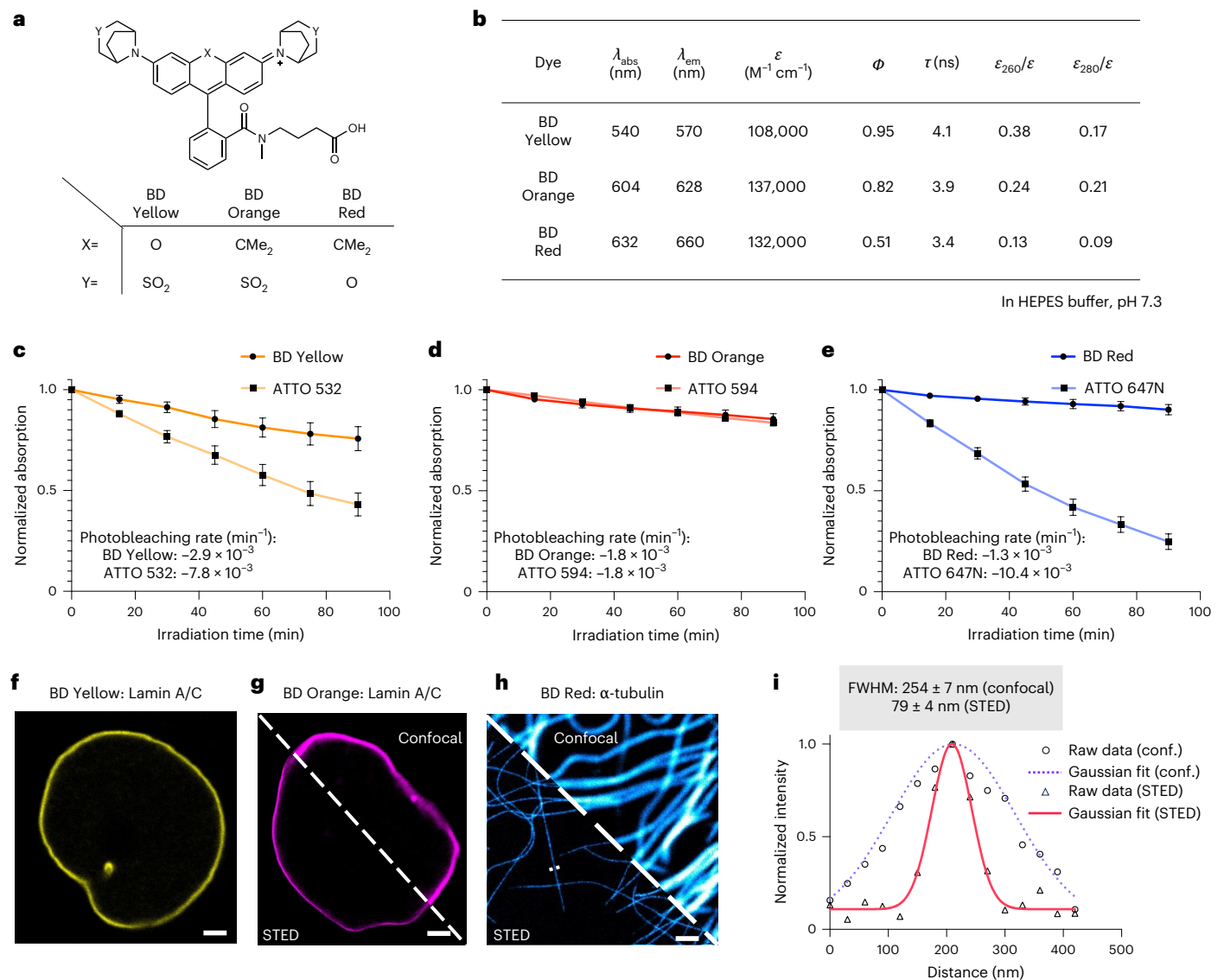


Fig. 3 | BD derivatives for antibody bioconjugation and immunofluorescence imaging. **a**, Chemical structures of BD derivatives for antibody bioconjugation. **b**, Photophysical properties of BD derivatives. ϵ_{260} , extinction coefficient at 260 nm; ϵ_{280} , extinction coefficient at 280 nm. **c–e**, Photobleaching curves of BD derivatives in HEPES buffer (10 mM, pH 7.3), ($n = 3$ independent experiments, data are shown as mean \pm s.d.). **c**, Absorption at λ_{max} of BD Yellow and ATTO 532, plotted as a function of irradiation time with an LED lamp at 520–530 nm. **d**, Absorption at λ_{max} of BD Orange and ATTO 594, plotted as a function of irradiation time with an LED lamp at 590–600 nm. **e**, Absorption at λ_{max} of BD Red and ATTO 647N, plotted as a function of irradiation time with an LED lamp at 620–630 nm. **f**, Confocal images of lamin A/C structures in fixed HeLa cells labeled by indirect immunofluorescence with a secondary antibody bearing BD

Yellow (DOL, 3.27). Scale bar, 2 μm . This experiment was independently repeated three times. **g**, Confocal (right) and STED (left) images of lamin A/C structures in fixed HeLa cells labeled by indirect immunofluorescence with a secondary antibody bearing BD Orange (DOL, 2.63). STED imaging was performed at at 775 nm (~ 120 mW). Scale bar, 2 μm . This experiment was independently repeated three times. **h**, Confocal (right) and STED (left) images of α -tubulin structures in fixed HeLa cells labeled by indirect immunofluorescence with a secondary antibody bearing BD Red (DOL, 2.42). STED imaging was performed at 775 nm (~ 140 mW). Scale bar, 1 μm . This experiment was independently repeated three times. **i**, Line-scan profile of fluorescence intensity at the dotted line in **h**, and a comparison of the full width at half maxima (FWHM) achieved under confocal and STED conditions ($n = 16$ filaments from 3 samples, data are shown as mean \pm s.d.).

higher brightness and photostability of BD566_{HTL}, the track lengths of single H2B molecules labeled by BD566_{HTL} (158 ± 6 s) were 1.7- and 4.3-fold longer than those labeled by JF549_{HTL} (95 ± 5 s) and TMR_{HTL} (37 ± 2 s), respectively (Fig. 4f). These data underscore the outstanding performance of BD566_{HTL} in cellular single-molecule imaging experiments.

We further assessed the performance of BD_{HTL} on bulk imaging experiments using HeLa cells stably expressing a nuclear-localized H2B–HaloTag7–GFP fusion protein (Fig. 4g). After 2 h of incubation at a 200 nM concentration with live HeLa cells, BD566_{HTL} exhibited 14% and 64% higher apparent brightness than JF549_{HTL} and TMR_{HTL}, respectively

(Fig. 4h). The labeling kinetics of nuclear HaloTag7 with BD566_{HTL} was about 50% slower than TMR_{HTL} owing to its slightly lower permeability attributed to its higher hydrophilicity (signal saturation within 30 min versus 20 min, Supplementary Fig. 10a). Owing to the differences in excitation spectra between CPY_{HTL} and BD626_{HTL}, a white light laser (WLL) was used to excite them at 620 nm for a comparable excitation efficiency. Under this condition, BD626_{HTL} showed 40% higher brightness than CPY_{HTL} (Fig. 4i,j). Similarly, BD666_{HTL} exhibited a better signal-to-background ratio compared to SiR_{HTL} (42.7 versus 23.0)⁴³ under the no-wash condition (Fig. 4k–l) and 36% higher brightness with a 658-nm excitation laser, at which channel the

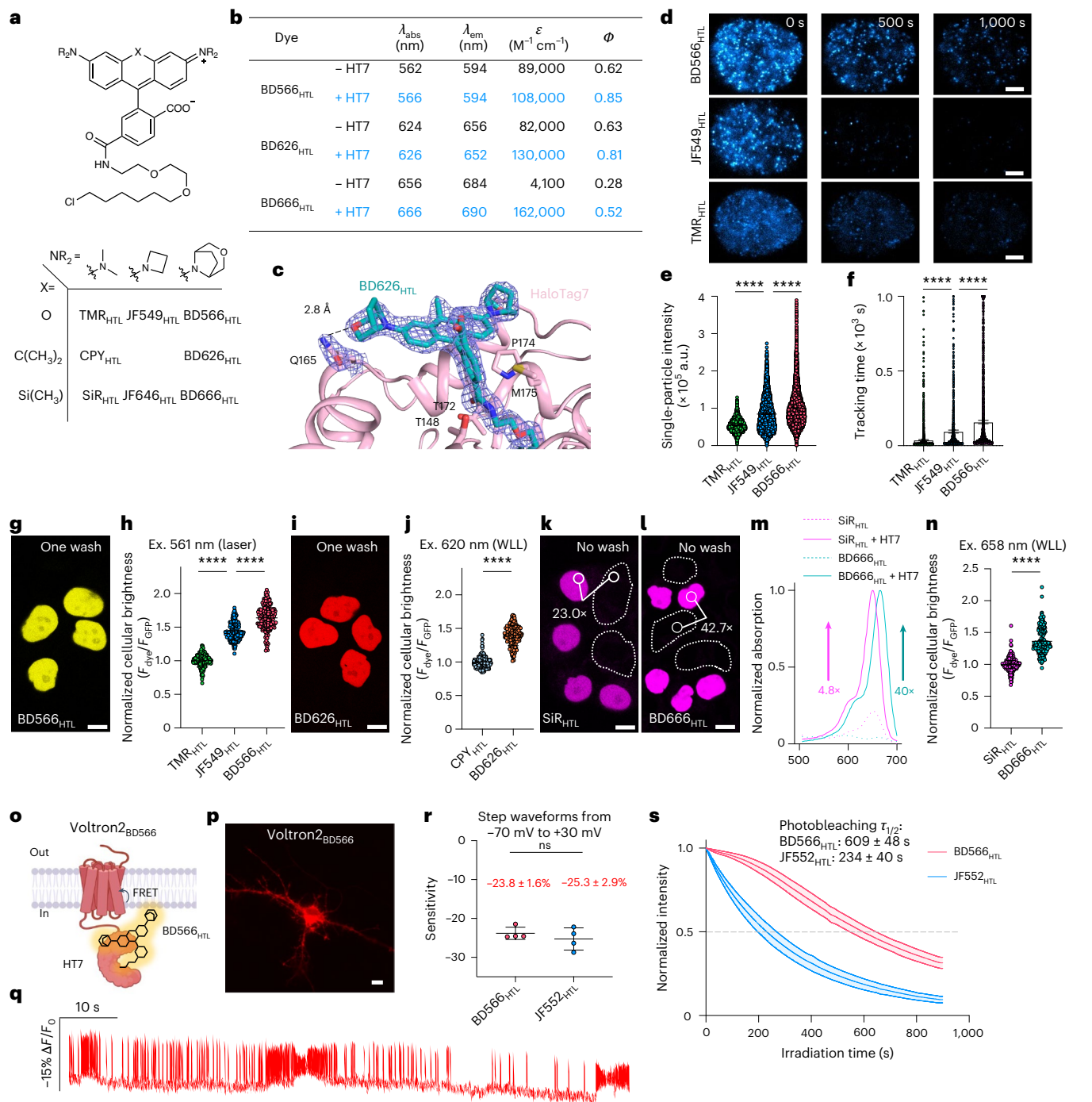


Fig. 4 | BD derivatives are exceptional HaloTag ligands for the labeling and imaging of cellular targets. **a**, Chemical structures of BD derivatives and their dimethyl/azetidine counterparts with HaloTag ligands. **b**, Photophysical properties of fluorescent HaloTag ligands. **c**, A close-up crystal structure of BD626_{HTL} in the pocket of HaloTag7, highlighting its polar interaction with Q165. The $2F_o - F_c$ omit electron density in the BD626_{HTL}-HaloTag7 complex crystal structure is contoured at 1.0σ . **d**, The indicated time points during continuous time-lapse single-molecule imaging of fixed U2OS cells stably expressing H2B-HaloTag7, labeled with tested dyes. Scale bars, 5 μm . **e**, Fluorescence intensity per particle per frame for tested dyes. For TMR_{HTL}, $n = 4,018$; JF549_{HTL}, $n = 7,464$; BD566_{HTL}, $n = 12,067$; data are shown as mean \pm s.e.m. a.u., arbitrary units. **f**, Tracking time of tested dyes. For TMR_{HTL}, $n = 1,924$; JF549_{HTL}, $n = 1,054$; BD566_{HTL}, $n = 1,909$; data are shown as mean with 95% confidence interval. **g, i, k-l**, Live-cell confocal images of HeLa cells stably expressing H2B-HaloTag7-GFP labeled with tested dyes; the signal-to-background ratio is given ($n = 130$ areas in 2 independent experiments). Scale bars, 10 μm . **h, j, n**, Comparison of apparent cellular brightness for various HaloTag ligands in two independent

experiments (data are shown as mean \pm s.d.). For TMR_{HTL}, $n = 189$ cells; JF549_{HTL}, $n = 194$ cells; BD566_{HTL}, $n = 170$ cells. For CPY_{HTL}, $n = 187$ cells; BD626_{HTL}, $n = 175$ cells. For SiR_{HTL}, $n = 176$ cells; BD666_{HTL}, $n = 191$ cells. Ex., excitation; F_{dye} , fluorescence signal from dye; F_{GFP} , fluorescence signal from GFP. **m**, Normalized absorption spectra of BD666_{HTL} and SiR_{HTL} in the presence or absence of excess HaloTag7 protein ($n = 2$ independent experiments). **o**, A cartoon of chemogenetic voltage sensor Voltron2_{BD566}. **p**, A representative wide-field image of a cultured rat hippocampal neuron expressing Voltron2 and labeled with BD566_{HTL}. Scale bar, 10 μm . This experiment was independently repeated three times. **q**, Fluorescence trace of voltage imaging recorded from a neuron prepared in **p**. **r**, Comparison of the voltage sensitivities between BD566_{HTL} and JF552_{HTL} on Voltron2 in HEK293T cells. $n = 4$; data are shown as mean \pm s.d. **s**, Normalized fluorescence decay curves of Voltron2 labeled with tested dyes during time-lapse confocal imaging on fixed neurons, $n = 4$ cells in two independent experiments; data are shown as mean \pm s.d. A two-sided unpaired Student's t -test was used to evaluate the significance of the mean. **** $P < 0.0001$. Exact P values are provided in Supplementary Table 1.

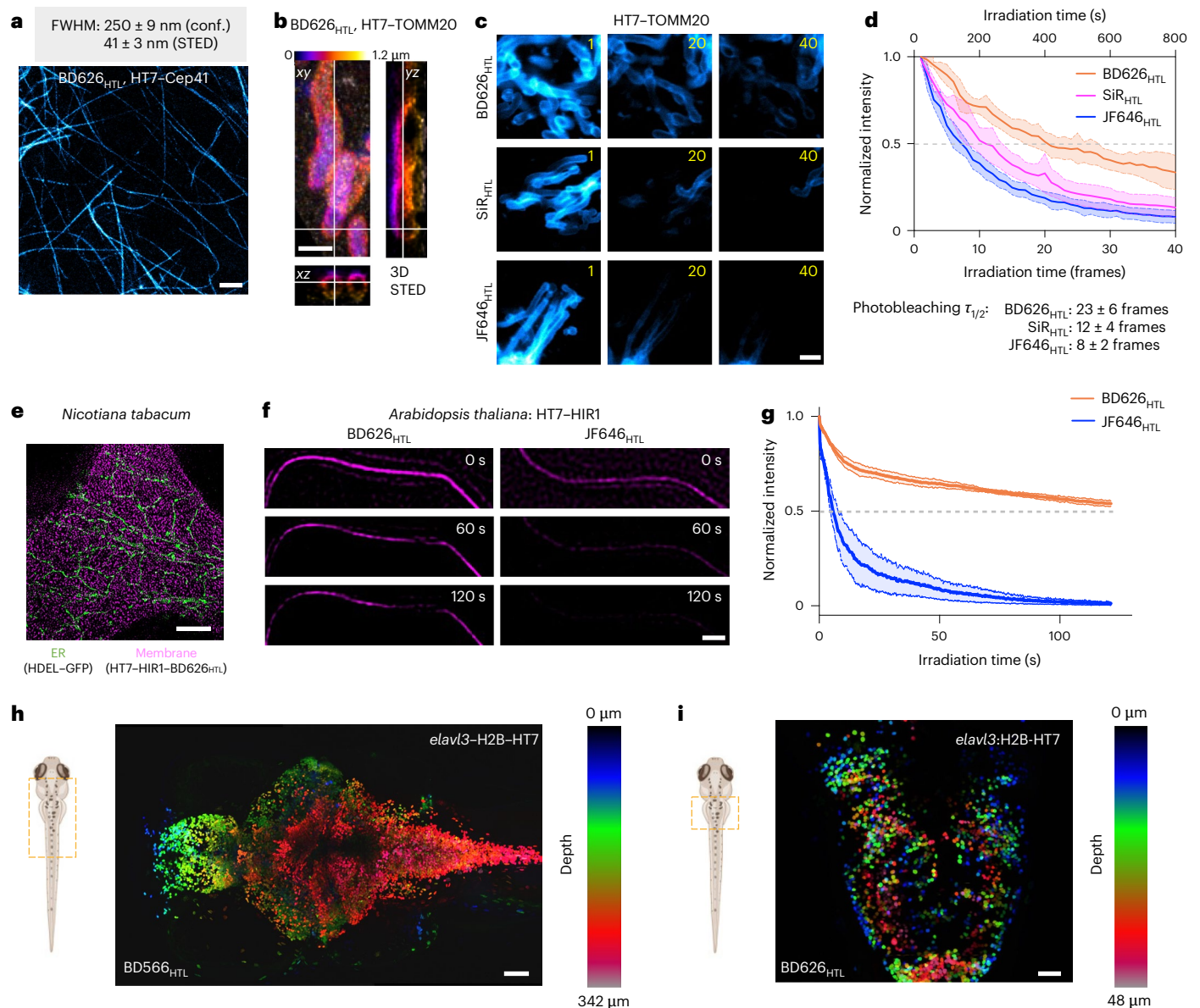


Fig. 5 BD_{HTL}s are versatile tools for general imaging in cells, plants, and animals. **a**, 2D-STED images of live HeLa cells expressing Cep41-HT7 labeled with BD626_{HTL}, and a comparison of the FWHM achieved under confocal (conf.) and STED (at 775 nm, -160 mW) conditions ($n = 15$ filaments from 3 samples; data are shown as mean \pm s.d.). Scale bar, 1 μ m. **b**, Orthogonal views of 3D-STED images of HeLa cells expressing TOMM20-HT7 labeled with BD626_{HTL}. A volume of $2.2 \times 5.8 \times 1.2$ μ m (xyz) was recorded using 30 z -stack images with a z -step of 40 nm. Scale bar, 1 μ m. This experiment was independently repeated three times. **c**, Time-lapse STED images of live HeLa cells expressing TOMM20-HT7 labeled with BD626_{HTL}, SiR_{HTL}, and JF646_{HTL}. Frame numbers are indicated at the top right corner. Scale bar, 1 μ m. **d**, Normalized fluorescence decay curves of samples in **c** with half-bleaching frame numbers (τ) given in brackets. $n = 6$ cells in two independent experiments; data are shown as mean \pm s.d. **e**, Two-color TIRF-SIM

images of live *N. benthamiana* cells expressing HDEL-GFP and HIR1-HT7 labeled with BD626_{HTL}. Scale bar, 5 μ m. This experiment was independently repeated two times. **f**, Time-lapse TIRF-SIM images of live *A. thaliana* cells expressing HT7-HIR1 labeled with BD626_{HTL} or JF646_{HTL}. Scale bar, 1 μ m. **g**, Normalized fluorescence decay curves of samples in **f**; $n = 4$ cells in two independent experiments; data are shown as mean \pm s.d. **h-i**, Z -stack confocal images of live zebrafishes expressing *elavl3-H2B-HT7* and labeled with BD566_{HTL} or BD626_{HTL}. This experiment was independently repeated three times. The dashed red square on the larval zebrafish outlines the imaged brain region. For **h**, the colored image shows the whole-body 3D reconstruction from 172 individual z -section images, with a z -step size 2 μ m. Scale bar, 100 μ m. For **i**, the colored image shows the 3D reconstruction of the hindbrain from 17 individual z -section images, with a z -step size of 3 μ m. Scale bar, 30 μ m.

excitation efficiencies were equivalent (Fig. 4n). There was no significant difference in cell permeability between CPY_{HTL} and BD626_{HTL} (Supplementary Fig. 10b); both fluorescence signals saturate within 2.5 min, which is also true for SiR_{HTL} and BD666_{HTL} (Supplementary Fig. 10c).

When imaged at the single-molecule level using a 642-nm excitation laser, BD626_{HTL}-labeled single H2B molecules exhibited brightness levels 1.30 and 2.18 times greater than those of SiR_{HTL} and BD666_{HTL} respectively (Supplementary Fig. 11a). In bulk experiments using a 640-nm excitation laser, BD626_{HTL} showed 352% higher brightness

than CPY_{HTL} (Supplementary Fig. 10b), yet BD666_{HTL} showed 49% lower brightness than SiR_{HTL} (Supplementary Fig. 10c). The differences in the above data are likely caused by the mismatch in excitation efficiency and cannot fairly compare the performance of BD_{HTL} with other dyes. However, these data are a valuable reference owing to the wide use of 640/642-nm lasers in fluorescence microscopy.

Encouraged by the outstanding performance of BD_{HTL} for the structural imaging of live cells, we further applied BD566_{HTL} to functional voltage imaging in cultured rat hippocampal neurons. We chose

the chemogenetic hybrid voltage sensor Voltron2 as a model, which contains a self-labeling HaloTag protein fused to the carboxy terminus of a voltage-sensitive rhodopsin (Fig. 4o)⁴⁹. Owing to the requirement of high-speed camera frame rate for voltage imaging, which typically exceeds 500 Hz, Voltron2-based sensors are very demanding in brightness and photostability for time-lapse data acquisition. Hippocampal neurons expressing Voltron2 can be readily labeled with BD566_{HTL}, resulting in a bright signal at the plasma membrane (Fig. 4p). Voltron2_{BD566} is capable of recording spontaneous neuronal action potentials with a sensitivity of approximately $11.32 \pm 0.69\%$ (Fig. 4q). There is no significant difference in the voltage sensitivities of BD566_{HTL} and JF552_{HTL} on Voltron2 (-23.8% versus -25.3%) in HEK293T cells (Fig. 4r). Compared to the spectrally similar Voltron2_{JF552}, Voltron2_{BD566} is 2.6 times more photostable as measured by half-bleaching time in fixed neurons ($\tau_{1/2}$, 609 s versus 234 s) (Fig. 4s). Together, the above voltage imaging data demonstrate that the brightness and photostability of Voltron2_{BD566} would make it an ideal sensor for the time-lapse recording of neuronal activity.

BD_{HTL} are powerful tools for imaging in cells, plants, and animals

Under confocal imaging, BD566_{HTL} and BD626_{HTL} exhibited high brightness, ideal permeability, high photostability, and high spectral stability, making them exceptional candidates for super-resolution imaging with enhanced illumination schemes. In live-cell time-lapse structured illumination microscopy (SIM) imaging, the fluorescence signal of BD566_{HTL}-labeled TOMM20-HaloTag7 retains more than 75% intensity after 100 frames (Extended Data Fig. 2). In live-cell STED microscopy, BD626_{HTL}-labeled microtubule-binding protein Cep41-HaloTag7 (Fig. 5a) showed markedly nanoscopic resolutions (41 ± 3 nm) under a 775-nm depletion laser (~ 160 mW). The resolution is comparable to that of SiR_{HTL} (50 ± 5 nm), which is recognized as one of the best dyes for live-cell STED imaging in the far-red channel (Supplementary Fig. 12). Live-cell STED time-lapse imaging further captured the dynamics of mitochondria (Fig. 5c and Supplementary Video 2). In this context, the number of frames with $>50\%$ original intensity ($\tau_{1/2}$) with BD626_{HTL} was around two times higher than that of SiR_{HTL} and three times higher than that of JF646_{HTL} (Fig. 5c,d). Furthermore, BD626_{HTL} enabled 3D STED imaging, a task previously hindered by repeated photobleaching during z-stacking. It provides >25 z-frames for 3D reconstruction, enabling the visualization of the complete 3D structure of mitochondrial outer membrane (Fig. 5b) or the distribution of the cytoskeleton (Cep41) throughout the entire cell (Extended Data Fig. 3). BD566_{HTL} and BD626_{HTL} are therefore recommended reagents for live-cell time-lapse nanoscopic and 3D imaging in red and far-red channels.

We then challenged whether the biocompatibility of BD dyes can enable super-resolution imaging in plants with cell walls, a crucial area that has been relatively underexplored with fluorescent dyes. The His-Asp-Glu-Leu (HDEL) endoplasmic reticulum retention signal is essential for correct folding and transportation of proteins^{50,51}, and the membrane hypersensitive induced reaction (HIR) protein plays a significant role in plant immunity⁵². We transiently expressed HDEL-GFP and HIR1-HaloTag7 in *Nicotiana benthamiana* leaves, which were incubated with BD626_{HTL}. Two-color total internal reflection SIM (TIRF-SIM) images show clear and specific signals of ER (HDEL) and membrane protein (HIR1) (Fig. 5e). We also expressed HIR1-HaloTag7 in another model plant cell: *Arabidopsis thaliana*. Live-cell time-lapse recording showed that BD626_{HTL} (Fig. 5f, left column) is ~ 20 times more photostable than JF646_{HTL} (Fig. 5f, right column) at the same channel ($\tau_{1/2}$, 121.2 s versus 6.2 s) (Fig. 5g and Supplementary Video 3).

Finally, we test whether BD dyes can freely diffuse into live zebrafish for in vivo imaging. Such an assay is challenging because the dye has to be sufficiently soluble to reach a high concentration for effective staining yet highly permeable to freely diffuse across

multiple membranes. Zebrafish larvae have transparent bodies and sophisticated nervous systems, making them ideal model animals for evaluating in vivo performance using fluorescence imaging. To this end, *elavl3*-H2B-GS-HaloTag plasmids were injected into fertilized zebrafish eggs, and labeling and imaging were conducted on the larvae at 4 and 5 days post fertilization, respectively. BD566_{HTL} and BD626_{HTL} ($3.3 \mu\text{M}$, 1 h) efficiently labeled the nuclear regions in the brain and spinal cord of live larvae under confocal microscopy. The abundant fluorescence signal allowed us to reconstruct the whole-body neural system in 3D (Fig. 5h-i and Supplementary Video 4). These whole-animal imaging experiments clearly demonstrate the in vivo labeling capability of BD_{HTL} dyes and their potential to advance neurobiological research, ranging from studies using cell models to live animals and spanning 3D structural imaging to long-time functional recordings.

Discussion

Here we establish SO₂⁻ and O-substituted azabicyclo[3.2.1]octane auxochromes as versatile molecular motifs to enhance fluorophores, achieving high brightness, exceptional photo-spectral stability, and tailored biochemical properties. From a chemical perspective, bridged bicycle-strengthened fluorophores represent a novel, modular, and integrated approach to probe design. The compact motif achieves five desired properties at once: (1) suppressing the formation of TICT states through steric hindrance and electronic effects, resulting in optimal fluorescence quantum yields; (2) blocking photooxidation pathways that form blue-shifted compounds, completely eliminating spectral artifacts in advanced imaging; (3) fine-tuning water solubility, cell permeability, K_{L-Z} values, and the spectra of fluorophores by introducing different hydrogen-bond acceptors into the azabicyclo[3.2.1]octane system, circumventing traditional modifications such as sulfonation; (4) pre-installing hydrogen-bond acceptors that interact with HaloTag and future engineered protein machinery; and (5) streamlining synthetic chemistry for easier preparations. We envision that this class of auxochromes will open new chemical space for fluorophore engineering^{53,54}.

From the perspective of bioimaging applications, the BD dye palette enables applications spanning antibody conjugation and immunofluorescence, live mammalian and plant cell labeling, chemogenetic sensors, and zebrafish labeling in vivo. Their superb optical properties are well suited for SIM and STED imaging, with rigorous neck-to-neck comparisons with widely used state-of-the-art fluorophores. With additional tuning and functionalization to further optimize the BD dye palette, such as fine-tuning the spectra²¹, balancing the lactone-zwitterion equilibrium^{55,56}, and alleviating phototoxicity⁵⁷, we anticipate that these bridged-bicyclic fluorophores will serve as infrastructure for advanced imaging applications, such as multiplexed single-molecule tracking, volumetric super-resolution imaging, and chemogenetic sensing (Extended Data Table 1).

Online content

Any methods, additional references, Nature Portfolio reporting summaries, source data, extended data, supplementary information, acknowledgements, peer review information; details of author contributions and competing interests; and statements of data and code availability are available at <https://doi.org/10.1038/s41592-025-02693-4>.

References

1. Sahl, S. J., Hell, S. W. & Jakobs, S. Fluorescence nanoscopy in cell biology. *Nat. Rev. Mol. Cell Biol.* **18**, 685–701 (2017).
2. Liu, Z., Lavis, Luke D. & Betzig, E. Imaging live-cell dynamics and structure at the single-molecule level. *Mol. Cell.* **58**, 644–659 (2015).
3. Sigal, Y. M., Zhou, R. & Zhuang, X. Visualizing and discovering cellular structures with super-resolution microscopy. *Science* **361**, 880–887 (2018).

4. Schermelleh, L. et al. Super-resolution microscopy demystified. *Nat. Cell Biol.* **21**, 72–84 (2019).
5. Wang, L., Frei, M. S., Salim, A. & Johnsson, K. Small-molecule fluorescent probes for live-cell super-resolution microscopy. *J. Am. Chem. Soc.* **141**, 2770–2781 (2018).
6. Schnermann, M. J. & Lavis, L. D. Rejuvenating old fluorophores with new chemistry. *Curr. Opin. Chem. Biol.* **75**, 102335 (2023).
7. Samanta, S. et al. Xanthene, cyanine, oxazine and BODIPY: the four pillars of the fluorophore empire for super-resolution bioimaging. *Chem. Soc. Rev.* **52**, 7197–7261 (2023).
8. Zhang, Y., Ling, J., Liu, T. & Chen, Z. Lumos maxima—how robust fluorophores resist photobleaching? *Curr. Opin. Chem. Biol.* **79**, 102439 (2024).
9. Sletten, E. M. & Bertozzi, C. R. Bioorthogonal chemistry: fishing for selectivity in a sea of functionality. *Angew. Chem. Int. Ed.* **48**, 6974–6998 (2009).
10. Koniev, O. & Wagner, A. Developments and recent advancements in the field of endogenous amino acid selective bond forming reactions for bioconjugation. *Chem. Soc. Rev.* **44**, 5495–5551 (2015).
11. Xue, L., Karpenko, I. A., Hiblot, J. & Johnsson, K. Imaging and manipulating proteins in live cells through covalent labeling. *Nat. Chem. Biol.* **11**, 917–923 (2015).
12. Saimi, D. & Chen, Z. Chemical tags and beyond: live-cell protein labeling technologies for modern optical imaging. *Smart Mol.* **1**, e20230002 (2023).
13. Giepmans, B. N. G., Adams, S. R., Ellisman, M. H. & Tsien, R. Y. The fluorescent toolbox for assessing protein location and function. *Science* **312**, 217–224 (2006).
14. Rodriguez, E. A. et al. The growing and glowing toolbox of fluorescent and photoactive proteins. *Trends Biochem. Sci.* **42**, 111–129 (2017).
15. Grimm, J. B. & Lavis, L. D. Caveat fluorophore: an insiders' guide to small-molecule fluorescent labels. *Nat. Methods* **19**, 149–158 (2021).
16. Panchuk-Voloshina, Nataliya et al. Alexa Dyes, a series of new fluorescent dyes that yield exceptionally bright, photostable conjugates. *J. Histochem. Cytochem.* **47**, 1179–1188 (1999).
17. Grabowski, Z. R., Rotkiewicz, K. & Rettig, W. Structural changes accompanying intramolecular electron transfer: Focus on twisted intramolecular charge-transfer states and structures. *Chem. Rev.* **103**, 3899–4031 (2003).
18. Wang, C. et al. Twisted intramolecular charge transfer (TICT) and twists beyond TICT: from mechanisms to rational designs of bright and sensitive fluorophores. *Chem. Soc. Rev.* **50**, 12656–12678 (2021).
19. Song, X. Z., Johnson, A. & Foley, J. 7-Azabicyclo[2.2.1]heptane as a unique and effective dialkylamino auxochrome moiety: demonstration in a fluorescent rhodamine dye. *J. Am. Chem. Soc.* **130**, 17652–17653 (2008).
20. Grimm, J. B. et al. A general method to improve fluorophores for live-cell and single-molecule microscopy. *Nat. Methods* **12**, 244–250 (2015).
21. Grimm, J. B. et al. A general method to fine-tune fluorophores for live-cell and in vivo imaging. *Nat. Methods* **14**, 987–994 (2017).
22. Grimm, J. B. et al. Optimized red-absorbing dyes for imaging and sensing. *J. Am. Chem. Soc.* **145**, 23000–23013 (2023).
23. Los, G. V. et al. HaloTag: a novel protein labeling technology for cell imaging and protein analysis. *ACS Chem. Biol.* **3**, 373–382 (2008).
24. Keppler, A. et al. A general method for the covalent labeling of fusion proteins with small molecules in vivo. *Nat. Biotechnol.* **21**, 86–89 (2003).
25. Helmerich, D. A., Beliu, G., Matikonda, S. S., Schnermann, M. J. & Sauer, M. Photobleaching of organic dyes can cause artifacts in super-resolution microscopy. *Nat. Methods* **18**, 253–257 (2021).
26. Dasgupta, A. et al. Effects and avoidance of photoconversion-induced artifacts in confocal and STED microscopy. *Nat. Methods* **21**, 1171–1174 (2024).
27. Grimm, J. B. et al. A general method to improve fluorophores using deuterated auxochromes. *JACS Au* **1**, 690–696 (2021).
28. Roßmann, K. et al. N-Methyl deuterated rhodamines for protein labelling in sensitive fluorescence microscopy. *Chem. Sci.* **13**, 8605–8617 (2022).
29. Ye, Z. et al. Quaternary piperazine-substituted rhodamines with enhanced brightness for super-resolution imaging. *J. Am. Chem. Soc.* **141**, 14491–14495 (2019).
30. Lv, X., Gao, C., Han, T., Shi, H. & Guo, W. Improving the quantum yields of fluorophores by inhibiting twisted intramolecular charge transfer using electron-withdrawing group-functionalized piperidine auxochromes. *Chem. Commun.* **56**, 715–718 (2020).
31. Butkevich, A. N., Bossi, M. L., Lukinavičius, G. & Hell, S. W. Triarylmethane fluorophores resistant to oxidative photobleaching. *J. Am. Chem. Soc.* **141**, 981–989 (2018).
32. Wang, L. G. et al. OregonFluor enables quantitative intracellular paired agent imaging to assess drug target availability in live cells and tissues. *Nat. Chem.* **15**, 729–739 (2023).
33. Corrie, J. E. T. & Munasinghe, V. R. N. Substituent effects on the apparent pK of the reversible open-to-closed transition of sultams derived from sulforhodamine dyes. *Dyes Pigm.* **79**, 76–82 (2008).
34. Grimm, J. B. & Lavis, L. D. Synthesis of rhodamines from fluoresceins using Pd-catalyzed C-N cross-coupling. *Org. Lett.* **13**, 6354–6357 (2011).
35. Zhang, J. et al. Red- and far-red-emitting zinc probes with minimal phototoxicity for multiplexed recording of orchestrated insulin secretion. *Angew. Chem. Int. Ed.* **60**, 25846–25855 (2021).
36. Walker, D. & Rogier, D. Preparation of novel bridged bicyclic thiomorpholines as potentially useful building blocks in medicinal chemistry. *Synthesis* **45**, 2966–2970 (2013).
37. Köbrich, G. Bredt compounds and the Bredt rule. *Angew. Chem. Int. Ed.* **12**, 464–473 (2003).
38. Wang, C. et al. Quantitative design of bright fluorophores and AIEgens by the accurate prediction of twisted intramolecular charge transfer (TICT). *Angew. Chem. Int. Ed.* **59**, 10160–10172 (2020).
39. Wang, B., Chai, X., Zhu, W., Wang, T. & Wu, Q. A general approach to spiro-lactonized Si-rhodamines. *Chem. Commun.* **50**, 14374–14377 (2014).
40. Kim, D.-H. et al. Blue-conversion of organic dyes produces artifacts in multicolor fluorescence imaging. *Chem. Sci.* **12**, 8660–8667 (2021).
41. Mujumdar, R. B., Ernst, L. A., Mujumdar, S. R., Lewis, C. J. & Waggoner, A. S. Cyanine dye labeling reagents - sulfoindocyanine succinimidyl esters. *Bioconjugate Chem.* **4**, 105–111 (1993).
42. Wurm, C. A. et al. Novel red fluorophores with superior performance in STED microscopy. *Opt. Nanoscopy* **1**, 1–7 (2012).
43. Lukinavičius, G. et al. A near-infrared fluorophore for live-cell super-resolution microscopy of cellular proteins. *Nat. Chem.* **5**, 132–139 (2013).
44. Butkevich, A. N. et al. Fluorescent rhodamines and fluorogenic carbopyronines for super-resolution STED microscopy in living cells. *Angew. Chem. Int. Ed.* **55**, 3290–3294 (2016).
45. Wilhelm, J. et al. Kinetic and structural characterization of the self-labeling protein tags HaloTag7, SNAP-tag, and CLIP-tag. *Biochemistry* **60**, 2560–2575 (2021).
46. Abdelfattah, A. S. et al. Bright and photostable chemigenetic indicators for extended in vivo voltage imaging. *Science* **365**, 699–704 (2019).
47. Huppertz, M.-C. et al. Recording physiological history of cells with chemical labeling. *Science* **383**, 890–897 (2024).

48. Tokunaga, M., Imamoto, N. & Sakata-Sogawa, K. Highly inclined thin illumination enables clear single-molecule imaging in cells. *Nat. Methods* **5**, 159–161 (2008).
 49. Abdelfattah, A. S. et al. Sensitivity optimization of a rhodopsin-based fluorescent voltage indicator. *Neuron* **111**, 1547–1563 (2023).
 50. Napier, R. M., Fowke, L. C., Hawes, C., Lewis, M. & Pelham, H. R. Immunological evidence that plants use both HDEL and KDEL for targeting proteins to the endoplasmic reticulum. *J. Cell Sci.* **102**, 261–271 (1992).
 51. Denecke, J., De Rycke, R. & Botterman, J. Plant and mammalian sorting signals for protein retention in the endoplasmic reticulum contain a conserved epitope. *EMBO J.* **11**, 2345–2355 (1992).
 52. Lv, X. et al. Membrane microdomains and the cytoskeleton constrain AtHIR1 dynamics and facilitate the formation of an AtHIR1-associated immune complex. *Plant J.* **90**, 3–16 (2017).
 53. Hara, D. et al. Silinanyl rhodamines and silinanyl fluoresceins for super-resolution microscopy. *J. Phys. Chem. B* **125**, 8703–8711 (2021).
 54. Lu, X. et al. Super-photostability and super-brightness of EC5 dyes for super-resolution microscopy in the deep near-infrared spectral region. *Chem. Mater.* **36**, 949–958 (2024).
 55. Grimm, J. B. et al. A general method to optimize and functionalize red-shifted rhodamine dyes. *Nat. Methods* **17**, 815–821 (2020).
 56. Wang, L. et al. A general strategy to develop cell permeable and fluorogenic probes for multicolour nanoscopy. *Nat. Chem.* **12**, 165–172 (2019).
 57. Liu, T. et al. Gentle rhodamines for live-cell fluorescence microscopy. *ACS Cent. Sci.* **10**, 1933–1944 (2024).
- Publisher's note** Springer Nature remains neutral with regard to jurisdictional claims in published maps and institutional affiliations.
- Springer Nature or its licensor (e.g. a society or other partner) holds exclusive rights to this article under a publishing agreement with the author(s) or other rightsholder(s); author self-archiving of the accepted manuscript version of this article is solely governed by the terms of such publishing agreement and applicable law.
- © The Author(s), under exclusive licence to Springer Nature America, Inc. 2025

Methods

Optical spectroscopy

UV-vis absorption and fluorescence. Fluorescent dyes were prepared as stock solutions in DMSO at a concentration of 1 mM and diluted such that the DMSO concentration did not exceed 0.5% (vol/vol). All measurements were taken at ambient temperature ($23 \pm 2^\circ\text{C}$) in 10 mM air-saturated HEPES buffer, pH 7.3, unless otherwise noted. The UV-vis absorption spectra of dye solutions were measured using a Deutta spectrometer (HORIBA Instruments) in a 3.5-ml square quartz cuvette (1 cm path length, Starna Cells). Emission spectra were measured using a Shimadzu RF-5301PC spectrofluorometer in the same cuvette. Normalized spectra are shown for clarity.

Extinction coefficient. Fluorescent dyes were quantified by quantitative nuclear magnetic resonance using a dioxane standard (2.0 μl). A dilution series of 0.5, 1.0, 1.5, 2.0, and 2.5 μM fluorophore was prepared in HEPES buffer (10 mM, pH 7.3) to determine the ϵ . The ϵ_{max} was measured in 0.1% (vol/vol) trifluoroacetic acid (TFA) in 2,2,2-trifluoroethanol (TFE) for the compounds BD528, BD555, TMR, BD586, BD615, and CPY, or 0.1% TFA in ethanol for compounds BD350, BD356, coumarin 460, BD623, oxazine 1, BD634, SiTMR, BD655, and SiR. Absorbance spectra were recorded on a Deutta spectrometer (HORIBA Instruments) and the absorbance maxima were plotted against the concentration. A linear function was fitted to the data using Origin 2023b, and ϵ values were calculated from slope following the Beer–Lambert law. Reported values for ϵ and ϵ_{max} are averages ($n = 3$).

Quantum yield. Absolute fluorescence Φ values were measured in HEPES buffer (10 mM, pH 7.3) using diluted samples (absorption < 0.1) on a FLS 980 lifetime and steady-state spectrometer (Instruments) that contained an integrating sphere to determine photons absorbed and emitted. Data were collected by Edinburgh Fluorade. Self-absorption corrections were performed using the instrument software. Reported values for Φ are averages ($n = 3$).

Fluorescence Lifetime. τ values were measured on a FLS 980 lifetime and steady-state spectrometer (Edinburgh Instruments). Measurements were conducted in HEPES buffer (10 mM, pH 7.3) for BD350, BD356, coumarin 460, BD528, BD555, TMR, BD615, CPY, BD623, oxazine 1, BD634, and SiTMR, and in 0.1% TFA in ethanol for BD586, BD655, and SiR. Single exponential fitting was performed using the instrument software to obtain τ values. Data were collected by Edinburgh Fluorade. Reported values for τ are averages ($n = 3$).

The lactone-zwitterion equilibrium constant. The lactone-zwitterion equilibrium constant $K_{\text{L-Z}}$ were calculated using the following equation, as reported⁵⁸:

$$K_{\text{L-Z}} = \frac{\epsilon_{\text{dw}}/\epsilon_{\text{max}}}{1 - \epsilon_{\text{dw}}/\epsilon_{\text{max}}} \quad (1)$$

ϵ_{dw} is the extinction coefficient of a fluorophore in a 1:1 spectral-grade dioxane (Sigma-Aldrich) to milliQ H_2O (vol/vol) solvent mixture. ϵ_{max} was measured in 0.1% (vol/vol) trifluoroacetic acid (TFA) in 2,2,2-trifluoroethanol (TFE) for BD528, BD555, TMR, BD586, BD615, and CPY, or 0.1% TFA in ethanol for BD655 and SiR.

Water solubility measurements

[2.2.1] Rhod, TMR, BD528, and BD555 were dissolved in 1 ml methanol, with the final stock concentration ranging from 10 to 50 mM. The solvent was removed in vacuo. After that, 250 μl double-distilled water was added. The mixture was vortexed and sonicated in an ultrasonic bath for 45 min at 95°C . The undissolved pellet was separated through centrifugation at 3,000g for 5 min. The concentration of dye in the supernatant was measured using a Deutta spectrometer (HORIBA Instruments) and then calculated using the Beer–Lambert law.

Bulk photobleaching

Fluorescent dyes were diluted with air-saturated HEPES buffer (10 mM, pH 7.3) to 10 μM , followed by irradiation with an LED lamp (520–530 nm, 0.5 W cm^{-2} for BD528, BD555, TMR, JF549, JF525, Rhod524, BD Yellow, and ATTO 532 (AAT-Bioquest: 2820); 590–600 nm 0.5 W cm^{-2} for BD615, CPY, BD Orange, and ATTO 594 (AAT-Bioquest: 2858); 620–630 nm, 0.5 W cm^{-2} for BD Red and ATTO 647N (AAT-Bioquest: 2854)). UV-Vis spectra were recorded on a microplate reader (TECAN Infinite M Nano⁺) in 96-well plates with optical bottoms (Costar) every 15 min over the course of 90 min. This experiment was independently repeated three times.

Nonspecific labeling of bovine serum albumin with dye photo-byproducts

JF549 and BD555 (10 μM) and BSA (5 mg ml^{-1}) were dissolved in 1 ml air-saturated PBS buffer (pH 7.4). The mixture was irradiated under an LED lamp (0.5 W cm^{-2} , 520–530 nm) for 30 min with continuous shaking. Afterwards, the samples were mixed with 5 \times loading buffer (LBP6510-10, COFITT) supplemented with 2-mercaptoethanol to a final concentration of 10%. Samples were heated for 5 min at 95°C , and a 10- μl aliquot of each sample was loaded into the gradient 4–15% Mini-PROTEAN TGX precast protein gels (Bio-Rad). SDS-PAGE was performed in Mini-PROTEAN Tetra Cell (Bio-Rad) apparatus, with the voltage set to 125 V, until the loading dye had run out of the gel. In-gel fluorescence was acquired with Bio-Rad Image System (Cy3 channel). Afterwards, the gels were stained with Coomassie Brilliant Blue G-250 for protein quantification. Image quantification was performed using Fiji software region measurement tool.

Computational chemistry

All calculations were carried out with Gaussian 16 software⁵⁹. The B3LYP functional⁶⁰ was adopted for all calculations in combination with the D3BJ dispersion correction⁶¹. For geometry optimization, frequency calculations and TD-DFT calculations, the 6-311G(d) basis set⁶² was used. The vertical ionization energies were further derived from single point calculations using the 6-311+G(d,p) basis set⁶³. The SMD solvation model⁶⁴ was used to take account of the solvation effect of water for all the calculations.

Cell biology

Cell culture. HeLa (HARVEYBIO, MB5422-S), COS-7 (HARVEYBIO, MB5841), and U-2 OS EF1 α -H2B-HaloTag7-expressing (gift from W. Deng's lab, Peking University) cells were cultured in Dulbecco's modified eagle medium (DMEM, 4.5 g L^{-1} glucose, Macgene catalogue number CM10017) supplemented with 10% (vol/vol) fetal bovine serum (FBS, Thermo Fisher Scientific catalogue number 10500064) and 1% (vol/vol) penicillin–streptomycin solution (10 IU ml^{-1} penicillin, 0.1 mg ml^{-1} streptomycin, Macgene catalogue number CC004) in a humidified 5% CO_2 incubator at 37°C . To prepare cells stably expressing histone H2B-HaloTag7-GFP, HeLa cells were integrated with an expressing plasmid through the PiggyBac transposase. Cells were split every 2–3 days or at confluency, and were regularly tested for mycoplasma contamination.

Transfection of cells. HeLa and COS-7 cells were transfected 24–48 h before imaging using lipofectamine 3000 (Thermo Fisher Scientific catalogue number L3000015). Transfection was carried out according to the manufacturer's protocols. After 6–12 h, the residual transfection reagent was removed and washed with DMEM. The cells were maintained in fresh medium for another 18–24 h before staining with dyes.

Fixation for immunofluorescence labeling. HeLa cells were grown for 48–72 h on glass coverslips and washed three times with PBS buffer (pH 7.4) before fixation. Cells were prefixed in 4% (vol/vol) formaldehyde (FA) in PBS for 45 s, permeabilized in 0.4% (vol/vol) Triton X-100 in PBS for 3 min, and fixed in 4% (vol/vol) PFA and 0.1% (vol/vol) glutaric

dialdehyde (GA) in PBS for another 15 min at 37 °C. PFA and GA were quenched by 100 mM NH₄Cl and 100 mM glycine in PBS for 10 min. After washing twice for 10 min in PBS, the cells were labeled with the corresponding antibodies.

Antibody labeling using NHS ester dyes

BD Yellow, Orange, and Red NHS esters (500 nmol) were dissolved in 20 µl DMSO. Then, the stock solutions were mixed with 1 mg secondary antibody (in PBS buffer, pH 8.3, adjusted by NaHCO₃ solution) in a proportion of 20–25 equivalents of dye to protein. After that, the mixture was incubated at room temperature for 2.5 h in the dark and was then purified using a gel filtration column (Sephadex G-25, Sigma-Aldrich). UV-Vis measurements were performed in a NanoDrop One small volume spectrometer (Thermo Scientific) to determine the degree of labeling (DOL, dye to protein ratio).

UV-Vis and fluorescence spectra of dye-HaloTag conjugates

HaloTag7 protein was recombinantly expressed and purified following an established protocol and stored as a 100 µM solution in 50 mM HEPES buffer containing 50 mM NaCl, pH 7.4. Fluorescent HaloTag ligands were diluted to 2 µM in 10 mM HEPES, pH 7.3. Then an aliquot of HaloTag7 protein (3.0 equivalents) was added, and the resulting mixture was incubated at 37 °C for 4 h. UV-Vis and emission spectra measurements were recorded on a microplate reader (TECAN Infinite M Nano⁺) in 96-well plates with optical bottoms (Costar). Reported values are averages ($n = 3$ independent experiments).

Cloning, protein expression, and purification

HaloTag7 was cloned in a pET21b(+) vector (Zoman) for production in *Escherichia coli*, featuring an amino-terminal His7 tag and a PreScission Protease (PP) cleavage site. Cloning was performed by Gibson assembly using *E. coli* DH5α cells (Beijing Zoman Biotechnology catalogue number ZC101). Proteins were expressed in *E. coli* strain BL21(DE3) (Beijing Zoman Biotechnology catalogue number ZC121). Lysogeny broth (LB) cultures were grown at 37 °C to an optical density at 600 nm (OD₆₀₀) of 0.8. Protein expression was induced by the addition of 1 mM isopropyl β-D-thiogalactopyranoside (IPTG), and cells were grown at 37 °C for 4 h and 18 °C overnight. The cells were centrifuged at 4,000g and 4 °C for 20 min. The pellet was collected and sonicated on ice in standard TBS buffer (20 mM Tris-HCl, 150 mM NaCl, pH 8.0) with 2 mM β-mercaptoethanol and 1 mM phenylmethanesulfonylfluoride (PMSF). Then, the cell debris was removed by centrifugation at 40,000g (JA-20, Beckman) at 4 °C for 30 min. The supernatant was loaded onto the TALON column (Clontech) and washed with 20 mM Tris-HCl (pH 8.0) and 500 mM NaCl, 2 mM β-mercaptoethanol, followed by TBS buffer with 10 mM imidazole. The column was eluted with 250 mM imidazole in TBS. The eluted protein was concentrated using Amicon Ultra 15-ml 10-kDa centrifugal filters (MilliporeSigma), and loaded onto a Superdex200 10/300 GL column (Cytiva) in TBS buffer, followed by purification with ÄktaPure chromatography system (Cytiva). The N-terminal His7 tag was removed by overnight cleavage with self-purified GST tagged PreScission Protease at 4 °C. The proteins were further purified by affinity-tag purification using a 5 ml HisTrap FF crude column (Cytiva) and a GSTrap HP Column (Cytiva) on an ÄktaPure chromatography system (Cytiva), in which the flow-through fractions were collected. Proteins were further separated by size-exclusion chromatography (Superdex200 10/300 GL column, Cytiva) in a mobile phase of standard TBS buffer and concentrated using Amicon Ultra 15-ml 10-kDa centrifugal filters (MilliporeSigma). Protein purity was verified through SDS-PAGE. Proteins were aliquoted and stored at –80 °C after being flash-frozen in liquid nitrogen.

Protein labeling and crystallization

HaloTag protein labeling was performed 2 h at 37 °C at a final concentration of 10 µM (BD626_{HTL}) in the presence of 5 µM HaloTag7 protein.

The protein was concentrated with Amicon Ultra 15-ml 10-kDa centrifugal filters (MilliporeSigma), and the excess of fluorophore substrate was removed by a 5 ml HiTrap Desalting column (Cytiva). Dye-protein conjugates were further purified by size-exclusion chromatography (Superdex200 10/300 GL column, Cytiva) in a mobile phase of crystallization buffer (10 mM Tris-HCl, 100 mM NaCl, pH 8.0) and concentrated using Amicon Ultra 15-ml 10-kDa centrifugal filters (MilliporeSigma) to a final concentration of 30 mg ml⁻¹. Dye-protein conjugates underwent crystallization trials using different commercial screens by mixing in a protein solution/crystallization solution (1:1; 200 nl final volume) using a NT8 Drop Setter for Protein Crystallization (Formulatrix).

BD626_{HTL}-HaloTag7 crystallization

Crystallization was performed at 20 °C using the vapor diffusion method. Crystals of HaloTag7 labeled with BD626_{HTL} fluorophore substrate were grown by mixing equal volumes of a 30 mg ml⁻¹ protein solution in crystallization buffer (10 mM Tris-HCl, 100 mM NaCl, pH 8.0) and a reservoir solution containing 0.1 M sodium cacodylate (pH 7.3), 0.2 M ammonium sulfate, and 32% (mass/vol) PEG 8000. The crystals were briefly washed with a cryoprotectant solution consisting of the reservoir solution with glycol added to a final concentration of 20% (vol/vol) before being flash-cooled in liquid nitrogen. Single-crystal X-ray diffraction data were collected at 100 K in the X-ray crystallography facility at Tsinghua University (XtaLAB Synergy Custom FRX and a hybrid photon counting detector HyPix6000, Rigaku). The structure of HaloTag7 labeled with CPY_{HTL} was determined by molecular replacement (MR) using Phaser⁶⁵, and the coordinates of PDB 6Y7A as a search model. Geometrical restraints for BD626_{HTL} were generated using the JLigand⁶⁶ program in CCP4 (ref. 67). The final models were optimized in iterative cycles of manual rebuilding using Coot^{68,69} and refined using phenix.refine⁷⁰. Data collection and refinement statistics are summarized in Supplementary Table 2, and the model quality was validated with MolProbity⁷¹ as implemented in PHENIX⁷².

Confocal imaging

Confocal imaging was performed on a Leica SP8 FALCON microscope (Leica Microsystems) equipped with a Leica TCS SP8 X scan head, a SuperK white light laser (WLL), Leica HyD SMD detectors, and a ×100, 1.40-NA oil objective. Data were collected using the Leica LAS X platform. For Figure 4i, CPY_{HTL} and BD626_{HTL} were excited at 620 nm (WLL, 10% intensity, emission 625–657 nm). For Fig. 4k,l, SiR_{HTL} and BD666_{HTL} were excited at 658 nm (WLL, 10% intensity, emission 663–713 nm). Other selected images were acquired with an Abberior STEDYCON microscope (Abberior Instruments) equipped with 488 (4.4 µW, emission 500–550 nm)/561 (5.0 µW, emission 575–625 nm)/640 (8.5 µW, emission 650–750 nm) laser and a ×100, 1.4-NA oil objective. Data were collected by STEDYCON 7.1.53. The Leica microscope was equipped with a live cell incubator (Life Imaging Services, 37 °C).

Live-cell fluorescence signal, labeling kinetics, and signal-over-background ratio.

HeLa cell lines stably expressing histone H2B-SNAP-eDHFRL28C-HaloTag7-GFP were seeded. For TMR_{HTL} (Promega catalogue number G8251), JF549_{HTL} (Promega catalogue number HT1020), and BD566_{HTL}, cells were labeled with 200 nM dyes for 2 h at 37 °C and washed once with culture medium (DMEM) before imaging. For CPY_{HTL} (SpiroChrome catalogue number SC306) and BD626_{HTL}, cells were labeled with 200 nM dyes for 1 h at 37 °C and washed once before imaging. For SiR_{HTL} (SpiroChrome catalogue number SC506) and BD666_{HTL}, cells were labeled with 200 nM dyes for 1 h at 37 °C and directly used for imaging without a washing step. Cells were focused in the 488 channel, and signals from the 561 or 640 channels were collected. The fluorescence signal intensity was measured from 12 fields of view in 3 repeated experiments ($n \geq 150$ cells) and normalized to the green fluorescent protein signal to correct for expression levels.

P values were calculated using the T.TEST function in Microsoft Excel 16.88. Statistical charts were drawn using GraphPad Prism 9.5.1.

Live-cell labeling of kinetic experiments was performed using 200 nM dye in the staining medium. The cells were imaged every 10 min for TMR_{HTL} and BD566_{HTL} and 2.5 min for CPY_{HTL}, BD626_{HTL}, SiR_{HTL}, and BD666_{HTL}. The nuclear fluorescence intensity was quantified from a total of >100 cells in 3 individual experiments, averaged, and normalized to the initial and maximal fluorescence signal.

To determine the signal-over-background ratio, live HeLa cells stably expressing H2B-SNAP-eDHFR-L28C-HaloTag7-GFP and wild-type HeLa cells were coseeded (1:1) at 37 °C in a humidified 5% (vol/vol) CO₂ environment for 1–2 days. The cells were labeled with 200 nM of SiR_{HTL} and BD666_{HTL} and directly imaged after 60 min. The white dashed lines (Fig. 4g) indicate the wild-type HeLa cells, which were located on the basis of brightfield images. The fluorescence signal in nucleus (F_{nuc} : HeLa H2B-SNAP-eDHFR-L28C-HaloTag7-GFP cells) and cytoplasm (F_{cyt} : wild-type HeLa cells) was corrected by subtracting the average density of adjacent background regions. The F_{nuc} and F_{cyt} values were determined on the basis of 150 cells in 3 repeated experiments. Signal-over-background ratio is calculated as $F_{\text{nuc}}/F_{\text{cyt}}$.

STED imaging

STED imaging was performed on an Abberior Facility microscope (Abberior Instruments) equipped with a 640-nm laser and a $\times 60$, 1.4-NA oil objective. Pixel sizes of 20 nm were used for single-frame super-resolution imaging. BD Orange, BD Red, BD626_{HTL}, and control dyes were excited at 640 nm (8.5 μ W, emission 650–750 nm), and STED was performed using a pulsed depletion laser at 775 nm (–60 to 200 mW) with gating of 1–7 ns and a dwell time of 10 μ s. Data were collected by Abberior Imspector 16.1.7098. The fluorescence intensity was fitted using a Gaussian fit in Origin 2023b software, and FWHM was estimated.

For 3D STED imaging, BD626_{HTL} (500 nM, 30 min, 37 °C, one wash) were excited at 640 nm (10 μ W, emission 650–750 nm), and STED was performed using a pulsed depletion laser at 775 nm (–80 mW, 80% to two dimensions and 20% to 3D) with pixel sizes of 40 nm and a dwell time of 8 μ s.

For time-lapse STED imaging, BD626_{HTL} and control dyes (500 nM, 30 min, 37 °C, one wash) were excited at 640 nm (5 μ W, emission 650–750 nm), and STED was performed using a pulsed depletion laser at 775 nm (–60 mW) with pixel sizes of 30 nm, gating of 1–7 ns, and a dwell time of 10 μ s (20 s per frame).

SIM imaging

SIM imaging was performed on the Polar-SIM system from Airy Technology. The SIM is equipped with a wide-field objective lens (CFISR HP Apo TIRF $\times 100$, 1.49-NA, Nikon). BD566_{HTL} was excited at 561 nm (200 mW, 25%, emission 575–625 nm). The original images were captured using an sCMOS camera (Hamamatsu, Orca Flash 4.0 version 3). Images were then reconstructed using Airy SIM's specialized processing software.

Single-molecule imaging

Microscopy setup. All single-molecule tracking (SMT) experiments were conducted using a custom-built Nikon Ti2 microscope, as described previously⁷³. It was equipped with two EM-CCD cameras (Andor, iXon Ultra 897), a $\times 100$, 1.49-NA oil-immersion TIRF objective (Nikon apochromat CFI Apo TIRF $\times 100$ oil), a perfect focusing system (Applied Scientific Instrumentation), and a stable-top chamber that maintains 37 °C and 5% CO₂ (Tokai Hit). The HILO illumination was achieved by a Nikon TIRF module, multiple lasers (405 nm: maximum 140 mW, OBIS, Coherent; 560 nm: maximum 1 W, MPB; 642 nm: maximum 1.5 W, MPB) controlled by the AOTF system (AA Opto-Electronic, AOTFnc-VIS-TN), a multi-band dichroic mirror (405-, 488-, 561-, and 633-nm quad-band, Semrock) and emission filters (TMR_{HTL}, JF549_{HTL}, BD566_{HTL}: Semrock 593/40-nm band-pass filter; BD626_{HTL}, SiR_{HTL}, and BD666_{HTL}: Semrock 676/37-nm bandpass filter).

Cell labeling for SMT. U2OS stably expressing histone H2B-HaloTag fusion proteins were generated by coexpressing the PiggyBac EF1a-H2B-HaloTag-IRES-Neo vector with the PiggyBac transposase, followed by G418 selection (400 μ g ml^{–1}) for 2 weeks and verification through FACS sorting. U2OS cells were plated on 8-well Cellvis chambers (Cellvis catalogue number C8-1.5H-N) with number 1.5 high-performance cover glass and were cultured in the complete DMEM (Gibco, catalogue number C11995500BT) supplemented with 10% FBS (VisTech, catalogue number SE100-011) and 1% penicillin-streptomycin (Hyclone, catalogue number SV30010). To label Halo fusion protein in living cells, Halo-ligand-conjugated fluorescent dyes at the indicated final concentrations were added to culture medium (2.5 pM for TMR_{HTL}, JF549_{HTL}, BD566_{HTL}, BD626_{HTL}, SiR_{HTL}, and BD666_{HTL}) and incubated in a cell incubator for 30 min. The medium was then removed, and two rounds of incubation (30 min) with fresh medium were performed to remove free dyes and fixed cells with 500 μ l 4% paraformaldehyde after 30 min. In each step, the medium was prewarmed, and caution was taken to avoid detaching cells from the glass bottom.

Acquisition and analysis of SMT data. The slowSMT experiments used a long exposure time (500 ms) and continuous low-intensity laser illumination to capture the position of slow-moving molecules. Generally, each cell was captured for 2,000 frames with a 500-ms exposure time at 10% maximal excitation power. The microscope, laser lines, and camera integration were controlled using the Nikon NIS-Elements software. The slowSMT movies were analyzed using custom-made MATLAB scripts (https://gitlab.com/tjian-darzacq-lab/SPT_LocAndTrack) implementing a multiple-target tracking algorithm⁷⁴ to generate single-molecule trajectories. The settings used in the MATLAB scripts for slowSMT were as follows: localization error, $1 \times 10^{-6.25}$; deflation loops, 0; blinking (frames), 1; maximum competitors, 3; maximum diffusion coefficient ($\mu\text{m}^2 \text{s}^{-1}$), 0.7. For SPT brightness, intensity values from the first frame of the imaging experiment were analyzed. For SPT duration, the single-molecule trajectories of each cell were combined, and a survival curve was generated on the basis of the 1 – cumulative distribution function (1 – CDF) histogram.

Voltage imaging

Cell culture and transfection. HEK293T cells (Solarbio, catalogue number SCC-120511-1EA) were incubated in DMEM (Gibco) containing 10% vol/vol FBS (Gibco) at 37 °C with 5% CO₂. Cells were seeded in a 24-well plate and grown to 70–90% confluent for transfection. Then, 500 ng plasmid of Voltron2 and 1 μ l Lipofectamine 2000 reagent were mixed in Opti-MEM medium and added to the culture cell in DMEM for 4–8 h. After that, cells were digested by trypsin-EDTA (0.25%, Gibco), reseeded on a sterile 14-mm glass coverslip pre-treated with matrigel matrix, and incubated in complete medium for 24 h before BD566_{HTL} labeling.

Primary rat hippocampal neurons were digested from isolated from rat brains at postnatal day 0 and seeded on 12-mm glass coverslips precoated with 20 μ g ml^{–1} poly-D-lysine (Sigma) and 10 μ g ml^{–1} laminin (Gibco). Neurons were incubated at 37 °C with 5% CO₂ in neuronal culture medium (Neurobasal medium, B-27 supplement, GlutaMAX supplement, and penicillin-streptomycin). Neurons were transfected on day 8 in vitro. For each well of a 24-well plate, 500 ng plasmid of Voltron2 and 1 μ l Lipofectamine 3000 reagent (Invitrogen) were mixed in Neurobasal medium and then incubated neurons with the mixture for 45 min at 37 °C with 5% CO₂. Transfected neurons were labeled and imaged after 3–10 days.

Voltage imaging. Neurons expressing Voltron2 were labeled with BD566_{HTL} (100 nM in DMEM) at 37 °C with 5% CO₂ for 30 min. After that, neurons were gently rinsed three times with DMEM and were

transferred to Tyrode's buffer before imaging. Voltage imaging was conducted using an inverted microscope (Nikon-TiE) equipped with a objective CFI PlanFluor $\times 40$, NA-1.3 (Nikon), one laser line (561 nm, Coherent OBIS), and one scientific CMOS camera (Hamamatsu ORCA-Flash 4.0 v2). The microscope, lasers, and cameras were controlled by a custom-built software written in LabVIEW (National Instruments, 15.0 version). To record action potentials, fluorescence images were captured at a frame rate of 400 Hz, under $\sim 1.6 \text{ W cm}^{-2}$ 561 nm illumination. Image analysis was performed in MATLAB (version R2018b) and ImageJ/Fiji (version 1.53t).

To investigate photobleaching of BD566_{HTL} and JF552_{HTL} in cells, Voltron2 was transfected in HEK293T cells. Transfected cells were labeled with BD566_{HTL} and JF552_{HTL}, and cells were fixed with 500 μl 4% paraformaldehyde after 24 h. Cells were transferred to Tyrode's buffer and then illuminated with 561 nm ($\sim 2 \text{ W cm}^{-2}$) lasers.

Imaging of plant cells

A. thaliana ecotype Columbia-0 (Col-0) and *N. benthamiana* were used as the wild-type control. Constructs were introduced into plants through the floral-dip method of *Agrobacterium tumefaciens*-mediated transformation⁷⁵. Seeds were surface-sterilized using a 4:1 mixture of ethanol and H_2O_2 (70% ethanol:30% H_2O_2), then stratified at 4 °C for 24 h in the dark. *Arabidopsis* was grown for 4 days on 1/2 MS medium supplemented with 1% sucrose under a 16-h light–8-h dark (23 °C–25 °C) photoperiod before imaging. The leaves of 6-week-old *N. benthamiana* plants were coinfiltrated with equal volumes of different *Agrobacterium tumefaciens* strain combinations, and the images were captured after 2 days at 23 °C–25 °C.

Arabidopsis seedlings and *N. benthamiana* leaves expressing the HaloTag vector were transferred into centrifuge tubes and infiltrated with HaloTag ligand solution (200 nM JF646_{HTL} (Promega catalogue number HT1060), 200 nM BD626_{HTL}), which was incubated for 1 h in the dark at 23–26 °C. Careful washing for a minimum of 4 h or up to overnight in water was essential to minimize nonspecific background⁷⁶. For imaging, a 4-day-old seedling was used and placed on a 35-mm-diameter, 170- μm -thick cover glass slide. Live-cell imaging was carried out on a GE Healthcare Delta Vision OMX SR imaging system furnished with a high NA $\times 60$, 1.42-NA objective. The GFP fluorophore was excited at 488 nm (200 mW, 20%, emission 500–550 nm). JF646_{HTL} and BD626_{HTL} were excited at excited at 640 nm (200 mW, 5%, emission 650–700 nm). Reconstruction and image analysis of the TIRF-SIM images were executed using SoftWoRx v5.9 (GE).

In vivo confocal imaging in larval zebrafish

For zebrafish experiments, larvae at 4–6 days postfertilization (dpf) were used in this study. Zebrafish adults, embryos, and larvae were maintained at 28 °C in system water on a 14-h light, 10-h dark cycle. All procedures were approved by the Institute of Neuroscience, Chinese Academy of Sciences.

The *elavl3*-H2B-HaloTag plasmid (25 ng μl^{-1}), mixed with Tol2 transposase mRNA (25 ng μl^{-1}), was injected into fertilized embryos with a Nacre background at the one-cell stage to generate chimeric transgenic fish. Before imaging, larvae at 4 dpf were soaked in the dye solution (3.3 μM in system water) for 1 h. Afterward, they were placed back in clean system water for 2 h to wash off the surface dye, and then imaging was performed. An FV3000 confocal microscope (Olympus) equipped with a $\times 20$, 1.0-NA water-immersion objective was used on fish embedded in 2% agarose gel to obtain 1,024 \times 1,024-pixel z-stack images. BD566_{HTL} was excited at excited at 561 nm (1 W, 5%, emission 593/40 nm); The BD626_{HTL} was excited at excited at 633 nm (1.5 W, 5%, emission 676/37 nm).

Reporting summary

Further information on research design is available in the Nature Portfolio Reporting Summary linked to this article.

Data availability

All data associated with this study are presented in the main text or Supplementary Information. The raw high-performance liquid chromatography, mass spectrometry, and nuclear magnetic resonance spectroscopy data are provided in the Supplementary Information. The structure of HaloTag7 bound to BD626_{HTL} has been deposited in the Protein Data Bank (PDB 6Y7B).

The raw imaging data for Figures 4d, and 5c,f,h are provided as Supplementary Videos 1–4. All chemical probes reported in this work are available from the corresponding author upon reasonable request. Selected BD_{HTL} dyes are commercially available from Genvivo Biotech and Spirochrome. Source data are provided with this paper.

References

- Grimm, J. et al. A general method to fine-tune fluorophores for live-cell and in vivo imaging. *Nat. Methods* **14**, 987–994 (2017).
- Adamo, C. & Baorne, V. Toward. Reliable density functional methods without adjustable parameters: the PBE0 model. *J. Chem. Phys.* **110**, 6158–6170 (1999).
- Stephens, P. J. et al. Ab initio calculation of vibrational absorption and circular dichroism spectra using density functional force fields. *J. Phys. Chem.* **98**, 11623–11627 (1994).
- Grimme, S., Antony, J., Ehrlich, S. & Krieg, H. A consistent and accurate ab initio parametrization of density functional dispersion correction (DFT-D) for the 94 elements H–Pu. *J. Chem. Phys.* **132**, 154104 (2010).
- Krishnan, R. et al. Self-consistent molecular orbital methods. XX. A basis set for correlated wave functions. *J. Chem. Phys.* **72**, 650–654 (1980).
- Clark, T., Chandrasekhar, J., Spitznagel, G. W. & Schleyer, P. V. R. Efficient diffuse function-augmented basis sets for anion calculations. III. The 3-21+G basis set for first-row elements, Li–F. *J. Comput. Chem.* **4**, 294–301 (1983).
- Marenich, A. V., Cramer, C. J. & Truhlar, D. G. Universal solvation model based on solute electron density and on a continuum model of the solvent defined by the bulk dielectric constant and atomic surface tensions. *J. Phys. Chem. B* **113**, 6378 (2009).
- McCoy, A. J. et al. Phaser crystallographic software. *J. Appl. Crystallogr.* **40**, 658–674 (2007).
- Lebedev, A. A. et al. J.Ligand: a graphical tool for the CCP4 template-restraint library. *Acta Crystallogr. D* **68**, 431–440 (2012).
- Winn, M. D. et al. Overview of the CCP4 suite and current developments. *Acta Crystallogr. D* **67**, 235–242 (2011).
- Emsley, P. & Cowtan, K. Coot: model-building tools for molecular graphics. *Acta Crystallogr. D* **60**, 2126–2132 (2004).
- Emsley, P., Lohkamp, B., Scott, W. G., & Cowtan, K. Features and development of Coot. *Acta Crystallogr. D* **66**, 486–501 (2010).
- Afonine, P. V. et al. Towards automated crystallographic structure refinement with phenix.refine. *Acta Crystallogr. D* **68**, 352–367 (2012).
- Chen, V. B. et al. MolProbity: all-atom structure validation for macromolecular crystallography. *Acta Crystallogr. D* **66**, 12–21 (2010).
- Adams, P. D. et al. PHENIX: a comprehensive Python-based system for macromolecular structure solution. *Acta Crystallogr. D* **66**, 213–221 (2010).
- Hansen, A. S., Pustova, I., Cattoglio, C., Tjian, R. & Darzacq, X. CTCF and cohesin regulate chromatin loop stability with distinct dynamics. *eLife* **6**, e25776 (2017).
- Sergé, A., Bertaux, N., Rigneault, H. & Marguet, D. Dynamic multiple-target tracing to probe spatiotemporal cartography of cell membranes. *Nat. Methods* **5**, 687–694 (2008).

75. Clough, S. J. in *Transgenic Plants: Methods and Protocols. Methods in Molecular Biology* Vol. 286 (ed. Peña, L.) 91–101 (Humana Press, 2005).
76. Lang, C., Schulze, J., Mendel, R.-R. & Hänsch, R. HaloTag™: a new versatile reporter gene system in plant cells. *J. Exp. Bot.* **57**, 2985–2992 (2006).

Acknowledgements

This project was supported by funds from National Key R&D Program of China (2021YFF0502904 to Z.C.; 2020YFA0509502 to W.D.), the Beijing Municipal Science & Technology Commission (project Z221100003422013 to Z.C.), the Beijing National Laboratory for Molecular Sciences (BNLMS202407 to Z.C.), and the Natural Science Foundation of China (32170566 to W.D.). We thank L. Chen at Peking University for the guidance in analyzing crystal structures. We thank J. Lin for the assistance with plant-cell imaging. We thank P. Xi for assistance with SIM imaging. We thank the Tsinghua University Branch of China National Center for Protein Sciences (Beijing) and Tsinghua University Technology Center for Protein Research for the X-ray crystallography facility support. We thank S. Fan, L. Wang, and M. Li at the X-ray crystallography platform of National Protein Science Facility, Tsinghua University, Beijing, for their technical help. We thank the Metabolic Mass Spectrometry Platform at the IMM, the analytical instrumentation center of Peking University, the NMR facility of the National Center for Protein Sciences at Peking University, and the National Center for Protein Sciences at Peking University.

Author contributions

Z.C. conceived the study. J.Z. and P.C. performed the chemical synthesis and characterizations. J.Z. performed the photophysical tests. K.Z. solved the crystal structures of HaloTag7–BD626. J.Z., M.Z.,

and T.L. performed confocal and STED imaging. K.W., S.F., and X.Z. performed in vivo imaging. B.W. performed single-molecule imaging. S.Z. performed voltage imaging. H.Q. performed SIM imaging on plant cells. Y.M. performed chemical calculations. Y.S. performed photo-crosslinking experiments. Y.F. performed SIM imaging on mammalian cells. P.Z., W.D., Y.M., and Z. C. supervised the project. J.Z. and Z.C. wrote the paper.

Competing interests

Z.C., J.Z., and P. C. are the inventors of a patent on the bridged-bicycle strengthened fluorophores (CN2023108090626, patent pending), whose value could be affected by this paper. The other authors declare no competing interests.

Additional information

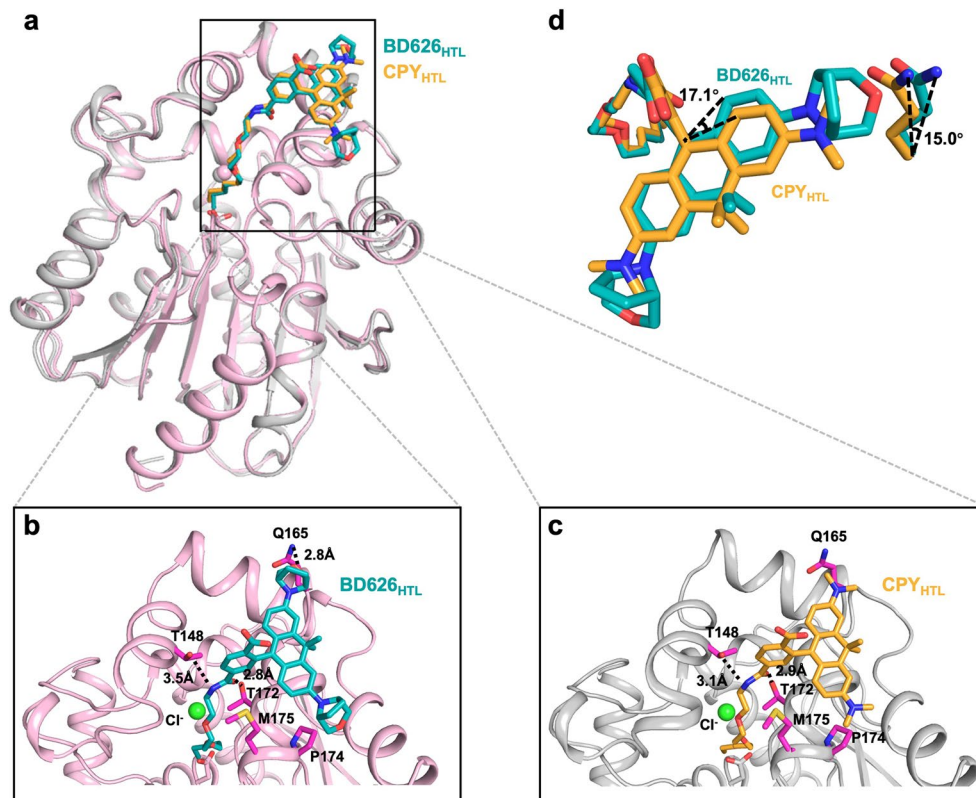
Extended data is available for this paper at <https://doi.org/10.1038/s41592-025-02693-4>.

Supplementary information The online version contains supplementary material available at <https://doi.org/10.1038/s41592-025-02693-4>.

Correspondence and requests for materials should be addressed to Zhixing Chen.

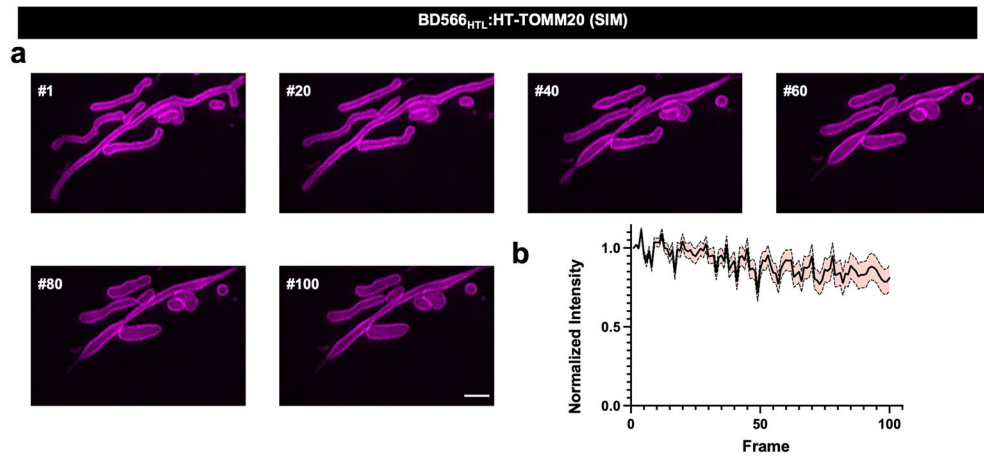
Peer review information *Nature Methods* thanks Lei Wang, Youjun Yang and the other, anonymous, reviewer(s) for their contribution to the peer review of this work. Primary Handling Editor: Rita Strack, in collaboration with the *Nature Methods* team.

Reprints and permissions information is available at www.nature.com/reprints.

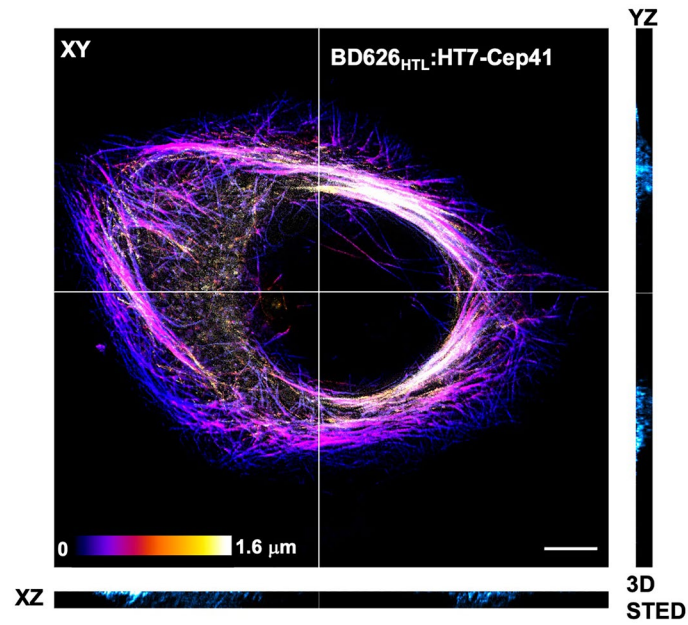


Extended Data Fig. 1 | A crystal structure of BD626_{HTL} at the HaloTag7 shows additional interactions between dye and protein. (a) Structural comparison between HT7-CPY (cyan, PDB 6Y7B) and HT7-BD626 (yellow, PDB 9JHA); (b-c) Close-ups of the substrate binding sites. Proteins are represented as pink

or gray cartoons. Fluorophores and residues are shown as sticks. A polar interaction is identified between the bridged auxochrome and Q165 and shown as dashed lines with annotated distances; (d) An overlaid comparison of CPY_{HTL} and BD626_{HTL} in the pocket of HT7.



Extended Data Fig. 2 | BD566_{HTL} enables time-lapse SIM imaging. (a) Time-lapse SIM images of live COS-7 cells stably expressing TOMM20-HT7 labeled with BD566_{HTL} (500 nM, 1 h, 37 °C, one wash), scale bar=2 μ m; (b) Normalized fluorescence decay curves of samples in (a), $n = 4$ in 2 independent experiments; error bar show \pm s.d.



Extended Data Fig. 3 | BD626_{HTL} can offer 25 z-frames for 3D reconstruction, enabling the construction of the distribution of the cytoskeleton (Cep41) throughout the entire cell. Orthogonal views of 3D-STED images of fixed HeLa

cells expressing Cpe41-HT7 labeled with BD626_{HTL} (500 nM, 30 min, 37 °C, one wash). An area of 52.5 × 51.0 μm (x–y) was recorded in 65 nm z-stacks over 25 times; scale bar = 1 μm.

Extended Data Table 1 | The major advantages BriDyes bring out in the manuscript by head-to-head comparisons

Figures	Assays	Fluorophores	Advantages of BriDyes
2l	Nonspecific protein crosslinking	BD555 v.s. JF549	Free from non-specific photocrosslinking
4c	Crystal Structure	BD626 _{HTL} v.s. CPY _{HTL}	New polar interaction between dye and protein
4d,e,f	Single-molecule imaging	BD566 _{HTL} v.s. JF549 _{HTL}	19% higher brightness 70% longer tracking lifetime > 3 folds counting lifetime Highest localization counts
4s	Voltage Imaging	BD566 _{HTL} v.s. JF552 _{HTL}	2.6 folds higher photostability
5b	3D STED	BD626 _{HTL}	>30 Z-stack images covering the entire mitochondria
ED 3	3D STED	BD626 _{HTL}	>25 Z-stack images covering cytoskeletal protein throughout the entire cell
5c&d	Time-lapse STED	BD626 _{HTL} v.s. SiR _{HTL} & JF646 _{HTL}	$t_{1/2}$: ~2 times longer than SiR _{HTL} /~3 times longer than JF646 _{HTL}
5g	SIM (plant cell)	BD626 _{HTL} v.s. JF646 _{HTL}	$t_{1/2}$: ~20 times longer than JF646 _{HTL}

Reporting Summary

Nature Portfolio wishes to improve the reproducibility of the work that we publish. This form provides structure for consistency and transparency in reporting. For further information on Nature Portfolio policies, see our [Editorial Policies](#) and the [Editorial Policy Checklist](#).

Statistics

For all statistical analyses, confirm that the following items are present in the figure legend, table legend, main text, or Methods section.

- | | |
|-------------------------------------|--|
| n/a | Confirmed |
| <input type="checkbox"/> | <input checked="" type="checkbox"/> The exact sample size (n) for each experimental group/condition, given as a discrete number and unit of measurement |
| <input type="checkbox"/> | <input checked="" type="checkbox"/> A statement on whether measurements were taken from distinct samples or whether the same sample was measured repeatedly |
| <input type="checkbox"/> | <input checked="" type="checkbox"/> The statistical test(s) used AND whether they are one- or two-sided
<i>Only common tests should be described solely by name; describe more complex techniques in the Methods section.</i> |
| <input checked="" type="checkbox"/> | <input type="checkbox"/> A description of all covariates tested |
| <input checked="" type="checkbox"/> | <input type="checkbox"/> A description of any assumptions or corrections, such as tests of normality and adjustment for multiple comparisons |
| <input type="checkbox"/> | <input checked="" type="checkbox"/> A full description of the statistical parameters including central tendency (e.g. means) or other basic estimates (e.g. regression coefficient) AND variation (e.g. standard deviation) or associated estimates of uncertainty (e.g. confidence intervals) |
| <input type="checkbox"/> | <input checked="" type="checkbox"/> For null hypothesis testing, the test statistic (e.g. F , t , r) with confidence intervals, effect sizes, degrees of freedom and P value noted
<i>Give P values as exact values whenever suitable.</i> |
| <input checked="" type="checkbox"/> | <input type="checkbox"/> For Bayesian analysis, information on the choice of priors and Markov chain Monte Carlo settings |
| <input checked="" type="checkbox"/> | <input type="checkbox"/> For hierarchical and complex designs, identification of the appropriate level for tests and full reporting of outcomes |
| <input checked="" type="checkbox"/> | <input type="checkbox"/> Estimates of effect sizes (e.g. Cohen's d , Pearson's r), indicating how they were calculated |

Our web collection on [statistics for biologists](#) contains articles on many of the points above.

Software and code

Policy information about [availability of computer code](#)

Data collection

Data analysis

For manuscripts utilizing custom algorithms or software that are central to the research but not yet described in published literature, software must be made available to editors and reviewers. We strongly encourage code deposition in a community repository (e.g. GitHub). See the Nature Portfolio [guidelines for submitting code & software](#) for further information.

Data

Policy information about [availability of data](#)

All manuscripts must include a [data availability statement](#). This statement should provide the following information, where applicable:

- Accession codes, unique identifiers, or web links for publicly available datasets
- A description of any restrictions on data availability
- For clinical datasets or third party data, please ensure that the statement adheres to our [policy](#)

All data associated with this study are presented in the main text or Supplementary Information. The raw high-performance liquid chromatography, mass spectrometry, and nuclear magnetic resonance spectroscopy data are provided as Supplementary Information. The structure of HaloTag7 bound to BD626HTL has been deposited in the Protein Data Bank (PDB 6Y7B).

The raw imaging data for Fig 4d, 5c, 5f and 5h are provided as Supplementary Video 1-4. Source data are provided with this paper.

Human research participants

Policy information about [studies involving human research participants and Sex and Gender in Research](#).

Reporting on sex and gender	<input type="text" value="N/A"/>
Population characteristics	<input type="text" value="N/A"/>
Recruitment	<input type="text" value="N/A"/>
Ethics oversight	<input type="text" value="N/A"/>

Note that full information on the approval of the study protocol must also be provided in the manuscript.

Field-specific reporting

Please select the one below that is the best fit for your research. If you are not sure, read the appropriate sections before making your selection.

Life sciences Behavioural & social sciences Ecological, evolutionary & environmental sciences

For a reference copy of the document with all sections, see nature.com/documents/nr-reporting-summary-flat.pdf

Life sciences study design

All studies must disclose on these points even when the disclosure is negative.

Sample size	<input type="text" value="No statistical method was used for sample size determination. More than two independent replicates of each experiments were performed. This sample size was resulted in low data variability. All quantitative imaging experiments were performed on replicate samples of fields of view as reported in Figure legends and supplementary materials."/>
Data exclusions	<input type="text" value="No data exclusion was performed."/>
Replication	<input type="text" value="The numbers of replicated experiments are indicated in the main text and figure legends."/>
Randomization	<input type="text" value="No randomization measures. The results of our experiments are quantitatively measurable parameters that are not influenced by subjective bias."/>
Blinding	<input type="text" value="No manual assessment of images was performed."/>

Reporting for specific materials, systems and methods

We require information from authors about some types of materials, experimental systems and methods used in many studies. Here, indicate whether each material, system or method listed is relevant to your study. If you are not sure if a list item applies to your research, read the appropriate section before selecting a response.

Materials & experimental systems

n/a	Involved in the study
<input type="checkbox"/>	<input checked="" type="checkbox"/> Antibodies
<input type="checkbox"/>	<input checked="" type="checkbox"/> Eukaryotic cell lines
<input checked="" type="checkbox"/>	<input type="checkbox"/> Palaeontology and archaeology
<input type="checkbox"/>	<input checked="" type="checkbox"/> Animals and other organisms
<input checked="" type="checkbox"/>	<input type="checkbox"/> Clinical data
<input checked="" type="checkbox"/>	<input type="checkbox"/> Dual use research of concern

Methods

n/a	Involved in the study
<input checked="" type="checkbox"/>	<input type="checkbox"/> ChIP-seq
<input checked="" type="checkbox"/>	<input type="checkbox"/> Flow cytometry
<input checked="" type="checkbox"/>	<input type="checkbox"/> MRI-based neuroimaging

Antibodies

Antibodies used	<input type="text" value="Goat anti-mouse IgG, Goat, HARVEYBIO, SR3459"/>
-----------------	---

Antibodies used	Lamin A/C monoclonal antibody, Mouse, Aladdin, Ab210151 alpha-Tubulin antibody, Mouse, Abcam, Ab52866
Validation	Antibodies were used without further validation as the obtained labeling was clearly compatible with the expected structures. No validation was required as antibodies were not used for epitope recognition.

Eukaryotic cell lines

Policy information about [cell lines and Sex and Gender in Research](#)

Cell line source(s)	HeLa, HARVEYBIO, MB5422-S COS-7, HARVEYBIO, MB5841 U-2 OS EF1alpha-H2B-HaloTag7, gift from Prof. Wulan Deng's Lab, Peking University HEK293T, Solarbio, SCC-120511-1EA HeLa H2B-HaloTag7-GFP, made by our Lab; HeLa cells were integrated with an expressing plasmid via the piggyback transposase.
Authentication	The cell lines were used without further authentication. Genetically modified cell lines clearly exhibited the expected labeling pattern.
Mycoplasma contamination	All cell lines tested negative for mycoplasma contamination.
Commonly misidentified lines (See ICLAC register)	No commonly misidentified cell lines were used in this study.

Animals and other research organisms

Policy information about [studies involving animals; ARRIVE guidelines](#) recommended for reporting animal research, and [Sex and Gender in Research](#)

Laboratory animals	Zebrafish larvae was of the species <i>Danio rerio</i> and were transgenic and used at 4-6. d.p.f.
Wild animals	No wild animals were used in this study.
Reporting on sex	The gender of zebrafish larvae cannot be determined thus sex was not considered in the experimental design.
Field-collected samples	No field-collected samples were used.
Ethics oversight	All the experiment procedures were approved by the Institutional Animal Care and Use Committee (IACUC) of the Institute of Neuroscience, Center for Excellence in Brain Science and Intelligence Technology, Chinese Academy of Sciences.

Note that full information on the approval of the study protocol must also be provided in the manuscript.